

Co-crystal engineering of a two-dimensional perovskite phase for perovskite solar modules with improved efficiency and stability

Received: 26 November 2023

Accepted: 17 October 2025

Published online: 31 December 2025

Narges Yaghoobi Nia  , Mahmoud Zendehdel  , Barbara Paci⁵, Jiayi Xu  , Marco Di Giovannantonio  , Amanda Generosi  , Enrico Leonardi⁷, Cong Liu  , Giorgio Contini⁵, Marco Guaragno⁵, Michael Grätzel  & Aldo Di Carlo  

 Check for updates

The use of two-dimensional perovskite interlayers enables high efficiency in perovskite solar cells and modules but presents challenges for their long-term operational stability. Here we use a co-crystal engineering approach to improve the long-term stability of these devices. We use a neutral molecule, benzoguanamine, as a linker in low-dimensional perovskites, replacing conventional ionic molecules, and form a co-crystal. By applying this co-crystal layer onto the perovskite layer, we achieve power conversion efficiency of 23.4% in small-area solar cells, and 23.1% and 18.5% on solar modules with active areas of 9.0 cm² and 48 cm², respectively. The solar modules retain more than 95% and 98% of their initial efficiency after >5,000 h of 1-sun light soaking and >1,000 h of ultraviolet-ray exposure, respectively, at maximum power point conditions. They also retain more than 91% of their initial efficiency after >5,000 h of continuous thermal stress at 85 °C.

In recent years, efforts in the perovskite solar cell (PSC) field have focused on improving long-term stability against light and thermal stresses, essential for industrial applications. Two-dimensional (2D) halide perovskites have emerged as superior to three-dimensional (3D) counterparts owing to their enhanced stability and versatility¹. The Goldschmidt tolerance factor and octahedral factor are critical in determining stable 3D or 2D perovskite phases², with 2D perovskites offering greater chemical engineering flexibility by relaxing the tolerance factor constraint. This flexibility enables precise control over key physical properties such as quantum confinement, dielectric confinement, structural distortion, exciton–phonon coupling and Rashba splitting, underscoring the potential of 2D perovskites across diverse applications^{3–5}.

The conventional 2D perovskite structure, described by the $(A')_m(A)_{n-1}B_nX_{3n+1}$ formula, features A' cations, either divalent ($m=1$) or monovalent ($m=2$), forming a bilayer or monolayer connecting the inorganic $(A)_{n-1}B_nX_{3n+1}$ 2D sheets. Tuning precursor composition adjusts the thickness of metal halide sheets, denoted by n value⁶. Bulky organic cations, either aliphatic or aromatic, are typically used at the A'-site to balance the charge of the BX_4^{2-} inorganic unit. Stable PSCs have been realized using various bulky cations⁷, with the best performances achieved by forming a 2D phase at the interface of 3D perovskite and the hole transport layer^{8–11}. Strong hydrogen bonding and π – π stacking interactions between bulky cations and inorganic layers significantly enhance the thermal and photostability of 2D perovskite structures^{12–14}. However, the ionic nature of bulky cations limits solvent selection

¹Iritaly Trading Company S.r.l., Rome, Italy. ²Laboratory of Photonics and Interfaces, Ecole Polytechnique Fédérale de Lausanne, Lausanne, Switzerland.

³Department of Electronics Engineering, University of Rome Tor Vergata, Rome, Italy. ⁴CHOSE, Centre for Hybrid and Organic Solar Energy, University of Rome Tor Vergata, Rome, Italy. ⁵CNR – Istituto di Struttura della Materia (CNR-ISM), Rome, Italy. ⁶Chemical Sciences and Engineering Division, Argonne National Lab, Lemont, IL, USA. ⁷Greatcell Italy, Greatcell Solar Italia, Rome, Italy. ⁸These authors contributed equally: Narges Yaghoobi Nia, Mahmoud Zendehdel.  e-mail: n.yaghoobinia@iritalytrading.it; mahmoud.zendehdel@uniroma2.it; aldo.dicarlo@uniroma2.it

for 3D/2D perovskite stack formation; protic polar solvents such as isopropyl alcohol can destabilize the 3D perovskite layer¹⁵, affecting performance and thickness during blade coating¹⁶. For better deposition of 2D overlayers, synthesized seeds of 2D crystals should dissolve in solvents with a dielectric constant >30 and a Gutmann number $5 < DN < 18 \text{ kcal mol}^{-1}$, as they cannot dissolve in non-polar solvents with <15 dielectric constant¹⁷. In 2D perovskites, charge-carrier extraction and mobility depend on film thickness, uniformity, phase purity, band alignment with the 3D layer and carrier-selective contact. Large organic cations insulated within 2D structures hinder charge transport and separation, impacting photovoltaic performance¹⁸. These cations may diffuse into the 3D bulk and fail to block ionic migration of volatile compounds such as MA^+ , altering interface properties and degrading cell performance under prolonged thermal and light stresses¹⁸. However, effective defect passivation in PSCs uses organic compounds such as Lewis acids, bases and zwitterions to enhance photovoltaic and stability performances¹⁹. However, non-ionic passivating molecules bond with 3D perovskite surface defects via self-assembly without forming a crystalline 2D phase, requiring an additional step to deposit bulky cations and achieve the 3D/2D crystalline structure's benefits.

Recent advancements in upscaling perovskite solar modules (PSMs) have used various scalable techniques^{20–25}. However, few reports^{21,26–29} have systematically evaluated the stability of high-efficiency PSMs using standard protocols such as ISOS and IEC61215. Although insights from PSCs can inform module-level stability, differences between PSCs and PSMs necessitate separate considerations²⁸. A critical factor for module stability is the impact of LASER processing in fabricating series-connected modules, which can affect stability owing to potential redox reactions between halide perovskite ionic moieties and various back contact metals³⁰, which can trigger the device degradation via ion migration. In addition, the selection of the hole transport layer is crucial, as it must be compatible with LASER processing and interface effectively with different metals. These factors highlight the complexities in scaling up PSMs and the ongoing challenges in achieving both high efficiency and long-term stability under practical conditions.

In this work, we develop a new strategy combining a new class of 2D perovskite interlayer and defect passivation through co-crystal engineering. We utilized 6-phenyl-1,3,5-triazine-2,4-diamine (benzoguanamine (BGA)) and 6-methyl-1,3,5-triazine-2,4-diamine (acetoguanamine (AGA)). These compounds served as neutral organic coformers (molecules that facilitate the formation of co-crystals through intermolecular interactions), leading to the formation of co-crystal 2D perovskite phases. Importantly, this process occurred without the need for any cation linker. The general formula for these phases is $(\text{L})_m(\text{A})_p\text{B}_n\text{X}_{3n+y}$, where L represents the neutral coformer ($0.125 \leq m \leq 0.5$), A is a small cation ($1 \leq p \leq 4$) and X is a halide ($0 \leq y \leq 3$). This approach resulted in the formation of two low-dimensional perovskite phases, including a Ruddlesden–Popper (RP)-like phase that preserved the initial perovskite stoichiometry during the 3D to 2D phase conversion. This method enhanced the stability and efficiency of PSCs and PSMs. Various experimental analyses and density functional theory (DFT) calculations suggested that the passivation mechanisms of this multifunctional 2D perovskite layer depend on the composition of the underlying 3D perovskite layer in which four stable stoichiometric co-crystal 2D perovskite phases can be obtained based on small cation concentration.

Low-dimensional co-crystal perovskite phases

Co-crystals combine different components within the same crystalline lattice through intermolecular bonding, allowing donor–acceptor (D–A) structures to form. This approach not only retains the intrinsic properties of the components but also introduces novel properties owing to the '1 + 1 > 2' effect^{31,32}. This makes co-crystal engineering advantageous for designing multifunctional materials such

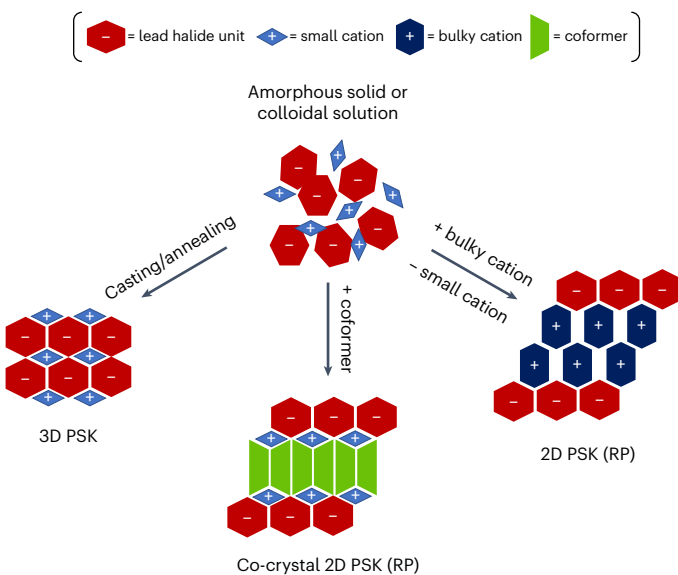


Fig. 1 | Co-crystal perovskite formation versus conventional structures.

A schematic representing the building block structure and forming process of a co-crystal 2D perovskite (PSK) with an RP-like crystalline morphology compared with the 3D perovskite and the conventional RP 2D perovskites, which are forming by ionic exchange with bulky cations as a linker.

as ambipolar charge transport, nonlinear optics and white light emission³³. In this study, we realized and developed a co-crystal engineering in organic/inorganic halide perovskite structures to form stoichiometric co-crystal 2D perovskite phases. Figure 1 illustrates the difference between a co-crystal 2D perovskite and the conventional 2D perovskites formed through ionic exchange reactions. By selecting an appropriate coformer, we were able to form an RP-like 2D perovskite phase without altering the previous perovskite stoichiometry during the 3D to 2D phase conversion. This method leverages the functional groups and molecular orbitals of the coformer within the 2D crystalline lattice for secondary chemical reactions and enhanced charge transport properties. Triazine derivatives, such as BGA and AGA, with a broad range of applications from general industry to biological activities^{34,35} are particularly effective for creating co-crystal phases owing to their strong intermolecular bonding capabilities³⁶. BGA and AGA, commercially available and well studied^{37,38}, use their amines, triazine nitrogen and π -orbitals to stabilize the crystalline lattice through hydrogen bonding and π - π stacking.

To verify the capability of BGA and AGA as the neutral molecules to form 2D perovskite crystalline thin films, we conducted various analyses on the thin-film structures of the stoichiometric phases of the BGA and AGA with different perovskite structures, including single-cation perovskite (MAPbI_3), double-cation perovskite (DCP) with general formulation of $\text{MA}_{0.10}\text{FA}_{0.90}\text{PbI}_{2.66}\text{Br}_{0.09}\text{Cl}_{0.25}$, triple-cation perovskite (TCP) with general formulation of $\text{Cs}_{0.05}\text{MA}_{0.15}\text{FA}_{0.8}\text{PbI}_{2.53}\text{Br}_{0.47}$ and lead iodide (PbI_2) in both states of composite 3D + 2D thin films (formed from mixed ink composition) and deposited double-layer 3D/2D perovskite films.

In order to study the 3D + 2D composite configuration of low-dimensional co-crystal thin films, we fabricated MAPbI_3 -based perovskite films on glass substrates using an antisolvent quenching method, incorporating different molar ratios of BGA, AGA or PEA⁺ (as a reference) linkers relative to lead (Pb). We adjusted the MA^+ concentration inversely to the linker concentration according to the formula $(\text{linker})_x\text{MA}_{1-x}\text{PbI}_3$, and also prepared and evaluated MA^+ -free samples with 1:1 and 2:1 linker/Pb ratios. From the X-ray diffraction (XRD) results, we found that unlike conventional ionic 2D perovskites where bulky cation concentration dictates crystallinity, in the BGA/AGA systems,

both the small cation (MA^+) concentration and the BGA/AGA molecular linkers control the crystalline orientation of the co-crystal 2D perovskite phase. Furthermore, we observed that adding even small amounts of BGA or AGA caused the diffraction peaks associated with the 3D perovskite phase in MAPbI_3 to shift to lower angles, an analysis that we conducted by following 6 main diffraction peaks representing different crystalline phases (Fig. 2a–d and Supplementary Fig. 1).

Specifically, increasing BGA or AGA concentration led to a progressive emergence and dominance of new low-angle peaks (around 5–8.5°) associated with layered structures, while the 3D alpha perovskite phase progressively decreased and eventually disappeared at high concentrations. In both the BGA and AGA systems, the presence of the small MA^+ cation was found to be crucial for forming these low-dimensional co-crystal structures, as MA-free samples only showed PbI_2 peaks. By contrast, the addition of the ionic PEA^+ linker showed that the [100] alpha perovskite peak still appeared even at high concentrations, and the formation of RP phases was observed in MA-free samples (Fig. 2c). The low-angle peaks and d -spacing values were further corroborated by grazing incidence wide-angle X-ray scattering (GIWAXS) analyses (Supplementary Fig. 2). The detailed discussion of the XRD results is available in Supplementary Note 1.

We used DFT and crystallography computations to investigate the interaction mechanisms of BGA and AGA linkers with perovskite materials, comparing them with the conventional ionic linker, PEA^+ . The analysis revealed that BGA and AGA molecules have evenly distributed frontier orbitals, which allows them to effectively passivate 2D perovskites. By contrast, PEA^+ has localized orbitals, which favour interactions with and stabilize 3D perovskites (Supplementary Figs. 3 and 4). This computational finding is consistent with the experimental XRD results. Further analysis showed that BGA binds most strongly at undercoordinated sites and in the interlayer region through N–H···I hydrogen bonding. Notably, BGA prefers a face-on orientation, a feature that could enhance charge transport (Supplementary Fig. 5). More detailed discussion about the computational baselines and relevant results is available in Supplementary Note 2.

Low-angle XRD peaks of co-crystal 2D perovskite samples were labelled using DFT calculations, XRD data and crystallography information files (CIFs) of similar phases^{39–42}. Peaks at diffraction angles of 20.5–5.5° and 5.5–6° correspond to [001] and [002] planes (primarily inorganic), while peaks at 2θ 6–7° and 7.5–8° correspond to [101] and [201] planes (with more organic contribution). As presented in Supplementary Fig. 6, from the stoichiometry calculations, we identified four feasible phases with increasing BGA linker concentration: $(\text{BGA})_{0.125}\text{MAPbI}_3$ (only [001] and [002]), $(\text{BGA})_{0.250}(\text{MA})_2\text{PbI}_4$ (all four peaks possible), $(\text{BGA})_{0.375}(\text{MA})_3\text{PbI}_5$ and $(\text{BGA})_{0.5}(\text{MA})_4\text{PbI}_6$ (maximum linker stacking).

Time-resolved photoluminescence (TRPL) analysis of MAPbI_3 films with varying BGA linker concentrations revealed a non-monotonic trend in carrier lifetime (Fig. 2d). A small 0.5% BGA addition significantly increased the TRPL decay time from 2.31 ns to 208.8 ns. Increasing the BGA ratio to 2% decreased the lifetime to 47.1 ns, but further increases led to a maximum lifetime of 304.5 ns at 10% BGA with the formula $(\text{BGA})_{0.1}(\text{MA})_{0.9}\text{PbI}_3$. Beyond this, the decay time generally decreased with higher BGA content, reaching drastically low values at $(\text{BGA})_{0.8}(\text{MA})_{0.2}\text{PbI}_3$, $(\text{BGA})\text{PbI}_2$ and $(\text{BGA})_2\text{PbI}_2$ compositions (4.1 ns, 2.2 ns and 1.0 ns, respectively), with minor increases observed at 40% and 50% BGA.

Fig. 2 | Structural and photophysical characterization of perovskite films with different linkers. a–c, Crystallinity variation of the different XRD angles versus changing of the linker/Pb molar ratio in the fabricated 3D + 2D perovskite thin films using BGA (a), AGA (b) and PEA^+ (c) as low-dimensional perovskite linkers. d, TRPL decay time comparison of 3D + 2D perovskite containing different BGA/Pb molar ratio. e, XRD patterns collected upon 3D/2D bilayer configuration of the samples with and without BGA as a 2D perovskite top layer. f, GIWAXS scattering

The surface morphology of MAPbI_3 thin films incorporating BGA and AGA linkers was examined via scanning electron microscopy (SEM) (Supplementary Figs. 7 and 8). Consistent with XRD findings, the SEM images revealed the formation of low-dimensional flakes on the film surfaces, with no such features observed in MA-free samples.

To understand the stoichiometry of co-crystal 2D perovskite phases with DCP and TCP, perovskite inks with varying BGA molar ratios were prepared and deposited. Ultraviolet-visible (UV-vis) spectroscopy of DCP-based films (Supplementary Fig. 9) showed a slight increase in absorbance with low BGA concentrations (1–2%), followed by a 3D perovskite onset decay at 25% BGA. At 50% BGA, 2D perovskite shoulders emerged (529 nm, 577 nm and 618 nm), and at 80% BGA, the 3D peak vanished, revealing 4 2D shoulders, with the 652 nm peak indicating $n = 4$ sheets⁴³. Conversely, TCP-based films showed no change at 1% BGA and a significant decrease in the 3D perovskite peak with higher BGA ratios, suggesting a weaker tendency for co-crystal 2D perovskite formation with BGA in TCP-based inks.

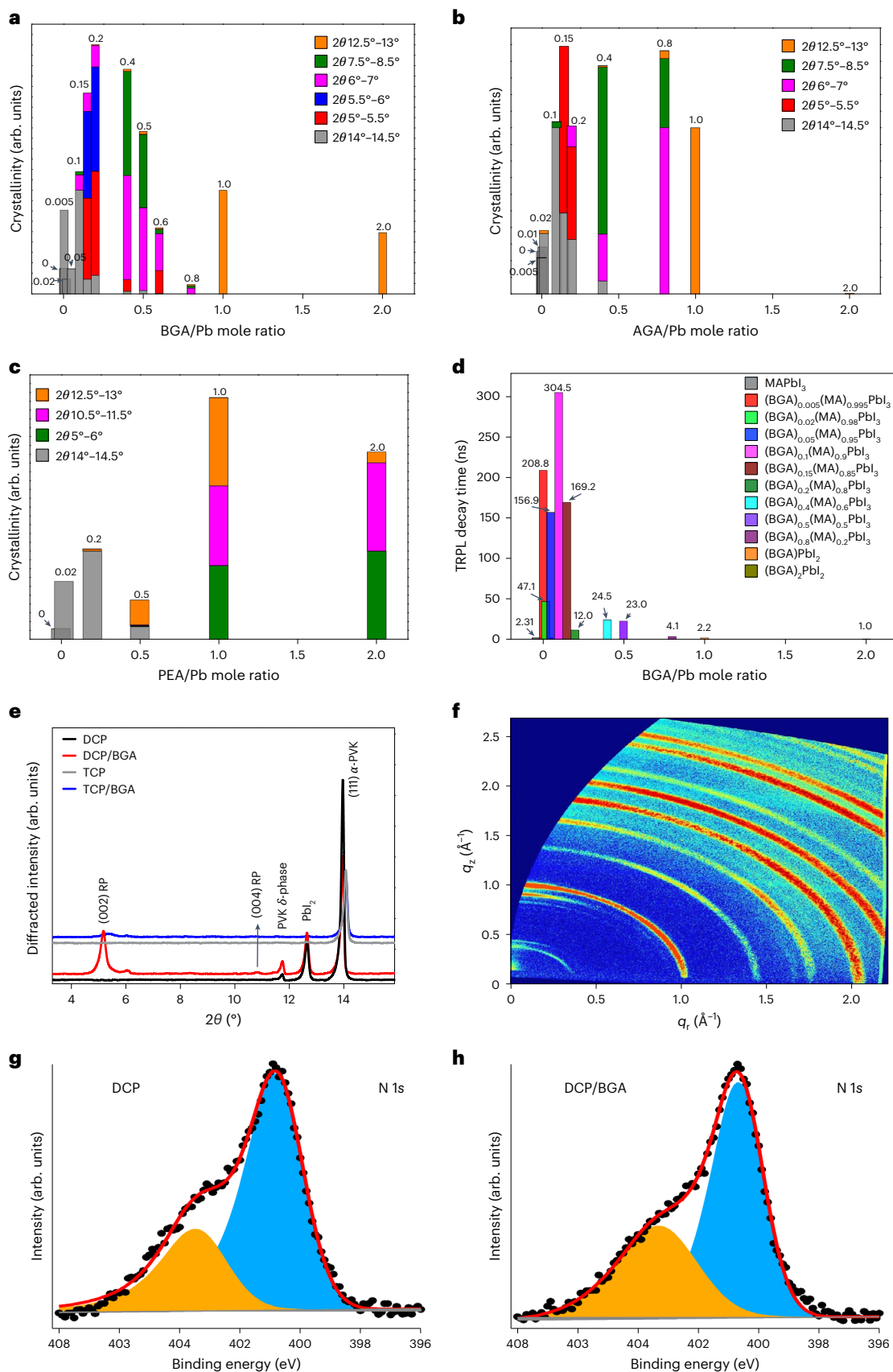
Photoluminescence (PL) analysis was performed on the perovskite films containing 80 mol% BGA, which exhibited prominent 2D perovskite features in their UV-vis spectra. Both films showed a broad PL emission peak around 575 nm, indicative of co-crystal 2D perovskite emission primarily from $n = 2$ sheets⁴³. In addition, we performed a control experiment to check the PL of the pure BGA molecules. Our results showed that the BGA-only film does not exhibit any emission peak in the measured range and the observation of the characteristic 2D perovskite emission in the BGA-containing perovskite films strongly support our interpretation that the BGA molecule plays a crucial role in the formation of the co-crystal 2D perovskite structure.

Owing to study the 3D/2D bilayer configuration of low-dimensional co-crystal thin films, DCP and TCP layers were formed on mesoscopic substrates using an antisolvent quenching method with optimized compositions. For 3D/2D samples, BGA solutions of varying concentrations (40 mM, 60 mM and 80 mM) in chlorobenzene (CB) were spin-coated on the perovskite films (Supplementary Fig. 9). Monitoring the 3D perovskite absorbance onset revealed slight changes with BGA concentration, differing between TCP/BGA and DCP/BGA films. In DCP/BGA films, absorbance increased with BGA concentration, suggesting potential enlargement of superficial 3D perovskite grains through defect passivation. Conversely, TCP/BGA films showed the opposite trend, indicating a different interaction mechanism.

Field emission scanning electron microscopy (FE-SEM) revealed changes in surface morphology upon BGA treatment (Supplementary Fig. 10). For TCP-based layers, BGA overlayers (40 mM and 80 mM) increased the average grain size from 230 nm in TCP to 430 nm and 320 nm, respectively, with some 100–200 nm 2D perovskite flakes observed. In DCP-based samples, BGA significantly impacted the surface by passivating grain boundaries, leading to larger superficial perovskite grains (from 580 nm in DCP to 1,400 nm and 1,500 nm with 40 mM and 80 mM BGA, respectively), with selective 2D perovskite flake formation at grain boundaries. These images suggest that BGA not only forms 2D perovskite flakes at defect points but also enlarges the 3D capping layer, likely owing to superficial recrystallization and grain boundary passivation, promoting grain merging⁴⁴.

XRD measurements at high and low scattering angles were conducted on 3D/2D perovskite layers in TCP/BGA and DCP/BGA stacks to gain structural information of the 2D perovskite overlayer. Supplementary Fig. 11 shows high-quality bulk alpha 3D perovskite for TCP-based

image of the DCP/BGA bilayer perovskite thin film. ‘ q_x ’ and ‘ q_z ’ represent the in-plane and out-of-plane components of the scattering vector, respectively. g, h, N1s XPS spectra from DCP (g) and DCP covered by BGA (h) thin films. Black dots represent experimental data, while the red lines result from the fit of the spectra with the filled-area Voigt (Gaussian/Lorentzian ratio of 80:20) components. A linear background subtraction was applied to both spectra.



samples, while DCP-based samples exhibit dominant cubic alpha perovskite⁴⁵ and a minor contribution of polymorphic delta phase⁴⁶ along with (001) PbI_2 signature. Low-angle XRD (Fig. 2e) revealed the same bulk perovskite and PbI_2 reflections, but also two low-angle diffraction peaks at $2\theta \approx 5.15^\circ$ and 10.40° in both TCP/BGA and DCP/BGA samples, indicative of layered 2D RP perovskite formation preferentially oriented parallel to the substrate⁴⁷. The detected reflection corresponds to the (002) RP peak ($n=1$)^{39,44,48}. Notably, BGA did not favour Dion–Jacobson 2D perovskite formation⁴⁹ consistent with its non-ionic nature and unique molecular orbitals. Qualitative analysis suggests enhanced RP phase crystallinity for DCP/BGA compared with TCP/BGA. The slight difference in the perovskite (111) peak could be due to different FA/MA ratios. The unchanged PbI_2 peak intensity in DCP and DCP/BGA indicates PbI_2 's non-participation in the co-crystal 2D perovskite phase formation.

GIWAXS analyses further confirmed the presence of low-angle peaks in the 3D/2D bilayer configuration, revealing diffraction arcs below 0.5 \AA^{-1} for DCP/BGA films, indicative of a low-dimensional structure (Fig. 2f). By contrast, DCP/PEA⁺ showed low-dimensional diffraction arcs around 0.5 \AA^{-1} , while the bare perovskite sample exhibited no low-angle diffraction signals (Supplementary Fig. 12).

X-ray photoelectron spectroscopy (XPS) analysis of DCP/BGA and DCP (reference 3D perovskite) revealed chemical state differences. N 1s, I 3d and Pb 4f core levels (Fig. 2g,h and Supplementary Fig. 13) showed aligned Pb 4f signals after normalization and energy alignment. All reported spectra were normalized to the photon flux, and energy aligned with respect to a reference gold sample, giving aligned Pb 4f signal for the two samples. N 1s spectra showed neutral (400.8 eV) and positive (403.4 eV) amine components^{50,51}. 3D/2D bilayer configuration showed increased neutral amine signal, indicating that bulk perovskite cations (FA^+/MA^+) are the source of positive amines. BGA contributes to the surface 2D perovskite without oxidation⁵² or cationic bonding, possibly through triazine ring electrons⁵³, supporting a co-crystal 2D phase with strong BGA intermolecular bonding. I 3d doublets were similar (-619.1 eV and 630.6 eV), with a minor -0.05 eV binding energy shift towards higher binding energy observed by using a fitting procedure for the DCP/BGA sample that can be tentatively attributed from H-bonding between BGA amines and iodine. Pb 4f signals showed two doublets (Pb 4f_{7/2} at 128.4 eV and 136.9 eV) with a slight change in relative abundance (DCP, 84%–16%; DCP/BGA, 80%–20%).

Photovoltaic performances and mechanism

The innovative BGA co-crystal 2D perovskite was used to fabricate PSCs and PSMs on 9.0 cm^2 and 48 cm^2 active areas. Three PSC types were fabricated: TCP/BGA and DCP/BGA double layers, and control DCP cells. Cross-section SEM images (Fig. 3a and Supplementary Fig. 14) of the DCP/BGA cell show a 1,036 nm perovskite layer with a 55 nm co-crystal 2D perovskite top layer, whose thickness varies depending on underlying grain boundaries, indicating preferential coverage of

surface defects. Achieving such selective defect coverage and measurable thickness is challenging with conventional cation-based 2D perovskite overlayers owing to protic solvent-induced exfoliation^{16,54}. However, BGA co-crystal engineering, using non-polar aprotic CB and BGA's multifunctional passivation, avoids this issue.

Statistical power conversion efficiency (PCE) results of fabricated PSCs are in Fig. 3b, with other photovoltaic (PV) parameters in Supplementary Fig. 15 (statistics from 12 cells per structure across three batches). Champion cell current density–voltage (J – V) curves are in Fig. 3c, and PV performance is in Table 1. The DCP/BGA champion cell achieved a significantly enhanced PCE of 23.4%, primarily owing to improved short-circuit current density (J_{sc}) and fill factor (FF) based on statistical data. Comparing BGA-coated devices with controls highlights the BGA co-crystal 2D perovskite layer's impact on FF, likely from selective defect passivation and better charge extraction to the hole transport layer, as supported by subsequent electrochemical and photophysical analyses. The champion device's Incident-Photon-to-Current Efficiency plot (Supplementary Fig. 16) shows good agreement between extracted current density and the J_{sc} from the J – V plot. On the basis of small-area cell J – V results and XRD stability tests (section 2.4), DCP was selected as the optimized 3D perovskite for further PSM investigation.

To investigate the impact of co-crystal 2D perovskite engineering on optoelectronic properties, TRPL decay was measured for the cells, and carrier lifetimes (τ) were extracted using a tri-exponential decay law (Fig. 3d). The co-crystal engineered cell exhibited a significantly longer carrier lifetime ($\tau = 302.1 \text{ ns}$) compared with the control cell ($\tau = 52.9 \text{ ns}$), approaching values observed in perovskite single crystals^{55,56}. The faster decay of the DCP cell arises from non-radiative recombination induced by defect states, while the slower decay of DCP/BGA is related to free carrier recombination⁵⁷, which demonstrates an effective suppression of the defects and the carriers' recombination after co-crystal engineering. Transient photovoltage (TPV) and transient photocurrent (TPC) responses were also analysed under varying light intensities (Fig. 3e,f and Supplementary Fig. 17). TPV decay showed a slower V_{decay} time of $130.0 \mu\text{s}$ for DCP/BGA versus $11.4 \mu\text{s}$ for DCP. Recombination times extracted from TPV (Fig. 3e) confirmed longer recombination times after co-crystal engineering, attributed to reduced perovskite surface recombination centres. TPC results (Fig. 3f) demonstrated enhanced hole extraction for the co-crystal engineered cells, with faster current density decay ($J_{decay} = 41.6 \mu\text{s}$) and higher collected charge compared with DCP ($J_{decay} = 55.6 \mu\text{s}$). This highlights the co-crystal 2D perovskite overlayer's effectiveness in improving charge extraction, likely owing to the face-on orientation of BGA facilitating charge transport through its π orbitals.

To understand the impact of the BGA 2D perovskite overlayer, we performed various electrochemical measurements on both modified and control devices. Electrochemical impedance spectroscopy (EIS) under dark conditions (Fig. 3g, Supplementary Fig. 18 and

Fig. 3 | Analysis of the impact of a 2D perovskite overlayer on the performance and charge dynamics of PSCs. **a**, Cross-section FE-SEM image from the DCP/BGA device (a part of the image has been coloured with 85% transparency for better distinction of the layers). **b**, Statistical PCE values of the PSCs containing a co-crystal 2D perovskite overlayer compared with DCP control cells (without any 2D overlayer). The statistic PCE data obtained from 12 independent devices for each studied configuration. The box plots presented as s.d. range with a coefficient of 1 and whisker in the outlier range and a coefficient of 1.5. The mean, min/max and 1%/99% percentages have been shown by the – and × symbols, respectively. **c**, J – V curves of the champion PSCs under AM1.5 G and sweeping the potential in both forward and reverse scan directions. **d**, Time-resolved PL decay profiles of the DCP/BGA and DCP cells. The PL decay was fitted to a triple-exponential model, with fitted lifetimes of $\tau = 302.1 \text{ ns}$ (reduced chi-squared 5.05×10^{-4}) and $\tau = 52.9 \text{ ns}$ (reduced chi-squared 3.01×10^{-4}) for co-crystal engineered and reference cells, respectively. **e**, Correlation of the recombination time and

voltage of the cells evaluated from TPV decay analysis. The TPV curves were fitted to a double-exponential model. **f**, Charge extraction curves of the cells extracted from TPC decay analysis. The charge is calculated by integrating the TPC decay curve (J – t curve), and the steady-state current density is taken at the end of each light pulse. **g**, Nyquist plots of the EIS results and equivalent fitting circuit of the DCP/BGA (fitting chi-squared 2.0×10^{-3}) and control DCP (fitting chi-squared 4.8×10^{-4}) devices under short circuit condition. Z and Z'' represent the real (resistive) and negative imaginary (capacitive) components of the complex impedance (Z), respectively. **h**, Dark J – V characteristics of the DCP and DCP/BGA devices plotted on a semi-logarithmic scale. The ideality factor (n) and saturation current density (J_0) were extracted from the linear region of the curves according to the Shockley diode equation. The reduced ideality factor ($n = 2.2$ versus 3.7) and lower saturation current (2.8 versus 5.3 nA cm^{-2}) for the DCP/BGA device confirm suppressed non-radiative recombination at the interfaces.

Supplementary Table 1) revealed key differences when analysed with a 3RC circuit model. This model associates high frequencies (CPE1/R1) with charge extraction and dielectric properties^{58,59}, intermediate frequencies (CPE2/R2) with interfacial recombination and low frequencies (CPE3/R3) with ion migration⁵⁸. Compared with the control, the co-crystal engineered device exhibited a decreased charge transfer resistance (R1), facilitating extraction. Critically, its recombination resistance (R2) was an order of magnitude higher, signifying suppressed recombination—likely owing to improved energy band alignment and greater quasi-Fermi level splitting induced by the BGA

layer⁵⁹. Furthermore, resistance to ion migration (R3) increased by three orders of magnitude, indicating a substantial enhancement in stability. These advantages persisted under applied bias voltages (Supplementary Fig. 18). The dark J - V characteristics (Fig. 3h) of the devices were analysed using the diode equation to extract the ideality factor (n) and saturation current (J_0)⁶⁰. The control DCP device exhibited a high ideality factor of $n = 3.7$, indicative of severe non-radiative recombination likely dominated by tunneling-assisted mechanisms or trap distributions at the heterojunction⁶¹. In contrast, the DCP/BGA device showed a significantly reduced ideality factor of $n = 2.2$.

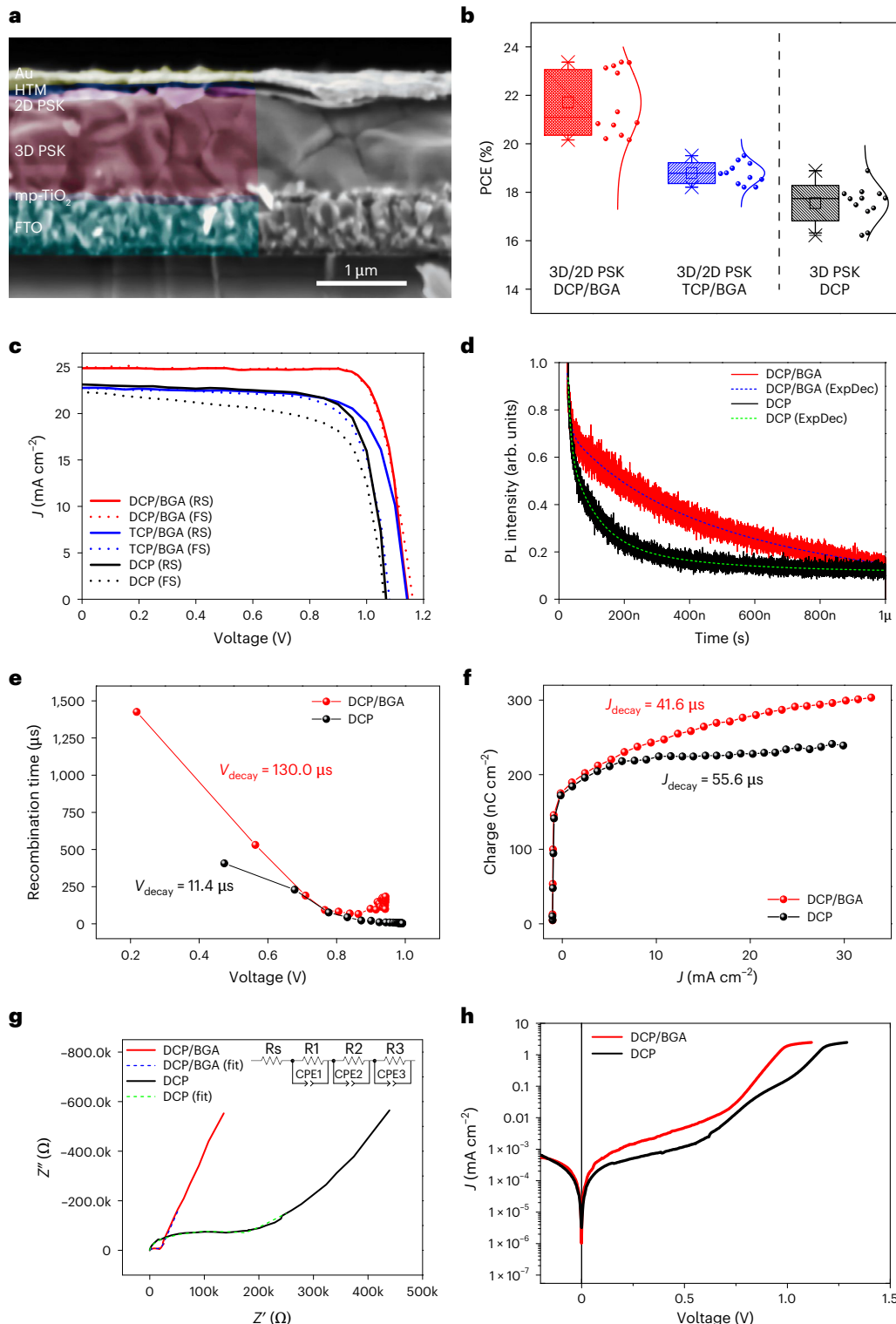


Table 1 | PV parameters of the PSCs with BGA as a co-crystal 2D perovskite overlayer compared with DCP-only control cells

Device		V _{oc} (V)	J _{sc} (mA cm ⁻²)	FF (%)	PCE (%)
DCP/BGA	Champion	1.16	24.9	81	23.4
	Statistic	1.10±0.05	24.5±0.2	80±2	21.6±1.4
TCP/BGA	Champion	1.14	22.8	75	19.5
	Statistic	1.08±0.03	22.7±0.3	77±2	18.8±0.4
DCP	Champion	1.07	23.1	76	18.8
	Statistic	1.05±0.01	23.3±0.4	72±2	17.5±0.7

This shift towards $n \approx 2$ suggests that the co-crystal engineering effectively suppressed the complex interface recombination channels, leaving standard trap-assisted recombination as the primary mechanism. Furthermore, the saturation current density decreased from 5.3 nA cm^{-2} to 2.8 nA cm^{-2} , confirming the reduction in leakage pathways and non-radiative losses, which aligns with the enhanced V_{oc} observed in the operational devices.

Collectively, these analyses show that the BGA 2D perovskite layer effectively enhances charge dynamics, reduces losses from recombination and traps, and improves stability against ion migration.

Following the concept of scalability (Fig. 4a), we fabricated PSMs of varying sizes using the optimized co-crystal engineered (3D/2D) structure. Details on the active area, laser patterning and design are provided in Supplementary Fig. 19. Initially, we created a batch of PSMs with a 9.0 cm^2 active area (91% geometrical FF (GFF), 5 series-connected cells) using the DCP/BGA structure, alongside control modules using only the DCP 3D perovskite. The co-crystal engineered modules exhibited excellent performance and reproducibility, achieving a champion efficiency (PCE) of 23.13% on the active area (Fig. 4c). Statistical analysis confirmed this high performance (Fig. 4b, Table 2 and Supplementary Fig. 20), which surpassed the control modules owing to improvements in all PV parameters. Encouraged by these results, we applied the DCP/BGA structure to fabricate larger module with an active area of 48 cm^2 (89% GFF). This larger module reached an active area PCE of 18.5% (Table 2 and Supplementary Fig. 21). Impressively, such a module is capable of generating over 886 mW of power under standard AM1.5 G illumination, showcasing the potential of this approach for large-area solar panel applications.

The stability of 9.0 cm^2 active area encapsulated modules was rigorously assessed under accelerated thermal (85°C , 65% relative humidity (RH)), 1-sun light soaking, both following ISO procedures⁶².

Fig. 4 | Large-area fabrication and enhanced stability of PSMs through co-crystal engineering. **a**, Picture of the fabricated modules with 9.0 cm^2 (5 series-connected cells with 0.5 cm width and 3.6 cm lengths of each cell) and 48 cm^2 (15 series-connected cells with 0.459 cm width and 7.0 cm lengths of each cell) active areas (a.a.). **b**, Statistic PCE values of the fabricated PSMs. The statistic PCE data obtained from 4 independent modules for each studied configuration. The box plots presented as s.d. range with a coefficient of 1 and whisker in the outlier range and a coefficient of 1.5. The mean, min/max and 1%/99% percentages have been shown by the – and × symbols, respectively. **c**, Current–voltage (IV)–PV curves of the champion modules with a 9.0 cm^2 active area. **d**, Thermal stability results of the encapsulated PSMs with a 9.0 cm^2 active area (the PCE values have been normalized divided by maximum and presented on the left y axis and the statistic PCE values have been presented on the right y axis with blue colour) under 85°C thermal stability test at ambient atmospheric conditions (~65% RH). The statistic PCE data obtained from 2 independent modules (the mean point and error bars of each measured time are presented in the statistic graph). **e**, The light soaking stability test results of the modules fabricated by DCP/BGA (initial PCE 19.25%) and DCP (initial PCE 18.73%) layers under MPP operation condition under 1-sun illumination and ambient atmospheric conditions (~65% RH).

and accelerated UV-ray exposure stability test. Impressively, co-crystal engineered modules showed exceptional thermal stability, achieving a T91 exceeding 5,000 h in damp heat tests (Fig. 4d), significantly outperforming control modules that lost 40% of their initial PCE after just 1,000 h. Detailed PV parameter analysis (Supplementary Fig. 22) indicated that the superior FF stability in co-crystal engineered modules, enabled by the BGA co-crystal 2D perovskite layer deposited from a non-polar solvent, was key to this enhanced thermal resilience.

In long-term light soaking tests (Fig. 4e), encapsulated DCP/BGA module maintained 95% of their initial PCE (19.25%) after over 5,000 h of 1-sun illumination, demonstrating remarkable photostability compared with the control modules that degraded by over 40% within 320 h. The initial PCE increase and subsequent partial decay observed in the co-crystal engineered modules up to 1,000 h are likely due to the effective ion migration blocking provided by the co-crystal 2D perovskite layer. This leads to the accumulation and stabilization of ions in the 2D layer, enhancing the 3D perovskite's built-in field through light-induced self-poling^{63–65}. The later slow PCE variations could arise from the dynamic ion movement between the 2D and 3D layers, possibly influenced by the self-repairing characteristics of the BGA coformer.

Furthermore, the encapsulated co-crystal engineered module demonstrated outstanding stability against continuous UV(A/B)-ray exposure, retaining over 98% of its initial efficiency (21.19%) after more than 1,000 h of maximum power point (MPP) tracking under ambient humidity (~65% RH) (Fig. 4f).

To illustrate the impact of our co-crystal approach on the stability of PSMs, Fig. 4g,h compares the stability of PSMs from the present work with literature results under continuous 1-sun light soaking (MPP tracking) and 85°C temperature stress, respectively. Our co-crystal engineering method shows a clear enhancement in both efficiency and stability compared with previously published results.

Owing to study the stability and passivation mechanism, in unencapsulated devices with a glass/fluorine-doped tin oxide (FTO)/mp-TiO_x/3D perovskite/2D perovskite/hole transport material (HTM) structure, the stability differences between a TCP/BGA and a DCP/BGA film were investigated under prolonged illumination in ambient conditions (25°C , 50% RH). According to Fig. 5, the TCP/BGA film degraded rapidly, with its 2D layer and alpha 3D phase disappearing and degradation products such as PbI₂ (001) and methylammonium iodide (MAI) (001) appearing. By contrast, the DCP/BGA film showed much slower degradation. The improved stability of DCP/BGA is attributed to the formation of a robust co-crystal 2D perovskite over-layer, which acts as a barrier against ion migration and enables defect self-repair, as evidenced by the persistence of MAPbI₃ polycrystalline markers despite the absence of alpha and delta phases after 1,000 h of illumination.

f, UV-ray exposure stability of encapsulated PSM with a 9.0 cm^2 active area fabricated by DCP/BGA (initial PCE 21.19%) under MPP tracking under continuous UV(A/B) exposure and ambient atmospheric conditions (~65% RH). **g,h**, Recent published reports about stability of the PSMs under continuous 1-sun light soaking (g) and 85°C thermal stability (h) tests compared with the present work. 1a 1,056 h T93.6 and 1b 1,000 h T91 of PSM with a champion PCE of 18.6% on a 29.5 cm^2 aperture area (20.2% PCE on an active area used in the figure)⁷⁵. 2a 1,000 h T91 and 2b 1,000 h T87 of PSM with an 18.8% champion PCE on a 17.1 cm^2 active area⁷⁶. 3a 1,000 h T90 and 3b 1,000 h T91 of PSM with an 18.5% efficiency on a 17.1 cm^2 aperture area⁷⁷. 4a 1,570 h T90 of PSM with a 16.6% PCE on a 22.4 cm^2 designated area²⁷. 4b 800 h T90 of PSM with a 17% PCE on a 43 cm^2 active area²¹. 5a 1,187 h T95 of PSM with a 16.6% PCE on a 20.77 cm^2 active area⁷⁸. 5b 1,000 h T95 and 6a 1,000 h T91 of PSM with a 15.6% PCE on a 36 cm^2 aperture area²⁶. 6b 3,260 h T90 of mini-module with a 14.4% PCE on a 1.92 cm^2 shadow masked area and a 4.32 cm^2 active area⁷⁹. 7a 388 h T80 of PSM with a 14.7% PCE on a 12 cm^2 active area⁸⁰. Compared with this work as 5,002 h T95 and 5,016 h T91 stability against continuous 1-sun light soaking and 85°C damp heat for the champion PSM with a 23.13% PCE on a 9.0 cm^2 active area.

Computational analysis using DFT supports these experimental findings, demonstrating that cation migration from the 3D perovskite is thermodynamically unfavourable in the presence of BGA, requiring an endothermic reaction energy of 0.56 eV (Supplementary Figs. 24 and 25). The BGA molecule enhances stability by passivating defects through Lewis adducts and strong intermolecular interactions such as H-bonding and π - π /C-H \cdots π interactions³⁶. A novel mechanism for the formation of the co-crystal 2D perovskite layer is proposed, based on a sequential process of ligand exchange reactions and intermolecular

bonding, rather than the conventional ion-exchange mechanism⁶⁶. This process, as depicted in Fig. 6, involves BGA displacing a halide to coordinate with Pb^{2+} and reorienting from an edge-on to a face-on configuration, which enables the formation of a stable co-crystal 2D perovskite phase with a single inorganic chain as the capping layer ($n=1$). The resulting 2D layer has the potential to block ion migration through the layer while enhancing charge-carrier mobility, which aligns well with the experimental interpretations and the promising long-term stability of DCP/BGA films and PSMs. The DFT calculations

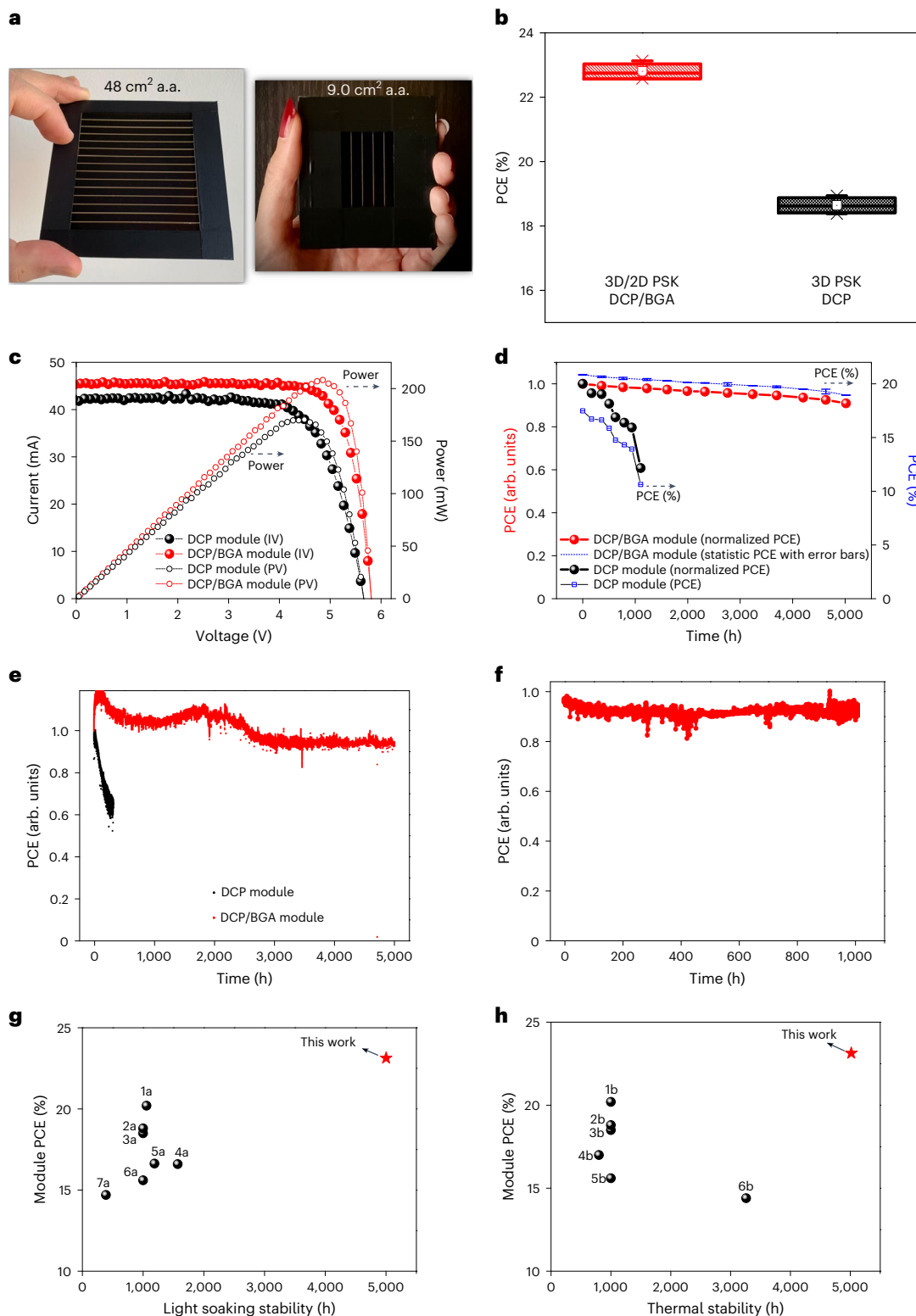


Table 2 | PV parameters of the PSMs with 9.0 cm² and 48 cm² active areas

PSM	a.a. (cm ²)	V _{oc} (V)	I _{sc} (mA)	FF (%)	PCE (%)
DCP/BGA	Champion	5.74	44.67	81.16	23.13
		5.74±0.02	44.1±0.5	81.3±0.4	22.8±0.2
DCP	9.0	5.60	41.31	73.66	18.94
		5.49±0.08	40.6±0.6	75.24±1.21	18.6±0.2
DCP/BGA	Champion	48	16.3	76.8	18.5

also show that BGA passivation at Pb and cation vacancy sites reduces the bandgap (Supplementary Fig. 26), and the energy level alignment of the complete device stack is presented in Supplementary Fig. 27. More detailed discussion about stability and passivation mechanism is available in Supplementary Note 3.

Conclusion

In summary, this study introduces BGA as a unique non-ionic coformer that assembles between organic–inorganic perovskite layers via strong intermolecular forces, creating a stable co-crystal 2D perovskite phase with improved photophysical properties owing to the face-on orientation and stabilized small cations. BGA's specific molecular orbital arrangement allows it to selectively passivate both halide and cationic vacancies by forming strong Lewis adducts and intermolecular bonds, acting as a multifunctional agent that preferentially covers defects owing to its solubility in non-polar aprotic solvents and functional group interactions. These BGA-based 2D perovskite films effectively block ion migration and the outgassing of volatile MA⁺ cations under prolonged ambient illumination. We proposed and validated a co-crystal 2D perovskite formation mechanism based on ligand exchange and intermolecular bonding. Utilizing a 3D/2D architecture with a double-cation 3D perovskite underlayer and a BGA-based co-crystal 2D perovskite overlayer, we achieved highly efficient PSCs (23.4% PCE) and stable modules (23.13% and 18.5% PCE for 9.0 cm² and 48 cm² active areas, respectively). Encapsulated co-crystal engineered modules demonstrated promising stability, exceeding 5,000 h T91 damp heat stability (85 °C, ~65% RH) and 5,000 h T95 light stability (1-sun, MPP, ~65% RH), consistent with ISOS and IEC61215 protocols. Furthermore, these modules showed high UV stability, retaining 98% efficiency after >1,000 h of MPP tracking under UV(A/B) exposure and atmospheric conditions (~65% RH). Thus, BGA represents a ground-breaking compound for realizing unique co-crystal low-dimensional perovskite phases using non-polar solvents, leading to highly efficient and stable perovskite devices. This work pioneers the realization and application of low-dimensional co-crystal phases in PSCs, potentially opening new avenues for crystalline phases in optoelectronic, photonic and electronic applications.

Methods

PbI₂ was purchased from Alfa Aesar; formamidinium iodide (FAI), methylammonium bromide (MABr) and methylammonium chloride (MACl) were purchased from Borun China; phenethylammonium iodide (PEAI) was purchased from Greatcell Solar; titanium dioxide paste (TiO₂-30 NRD) was purchased from Greatcell Solar; lead bromide (PbBr₂) was purchased from TCI Chemicals; (poly[bis(4-phenyl)(2,4,6-trimethylphenyl)amine] ultra-high molecular weight (PTAA) 390 kDa) was purchased from Solaris Chem; 4-*tert*-butylpyridine (TBP), bis(trifluoromethylsulfonyl)imide lithium salt (Li-TFSI), cobalt(III) tris(bis(trifluoromethylsulfonyl)imide) (FK-209), caesium iodide (CsI), *N,N*-dimethylformamide (DMF), dimethyl sulfoxide (DMSO), CB, diethyl ether (DEE), BGA, AGA and acetonitrile were purchased from Sigma-Aldrich; FTO (TEC 7) conductive glass was purchased from Pilkington. All the chemicals were used as received without further purification.

Small-area device fabrication

Patterned FTO substrates (four isolated cells in a 2.5 × 2.5 cm² substrate area) were cleaned using detergent aqueous solution (Hellmanex III (5% v/v) in ionized water), deionized water and 2-propanol, respectively (3 min each step) via an ultrasonic bath. A 50 nm of the compact TiO₂ (c-TiO₂) layer was deposited onto the patterned FTO via spray pyrolysis deposition at 460 °C using a previously reported procedure⁶⁷. A mesoporous TiO₂ layer was deposited on the c-TiO₂ by using a 1:7 w/w diluted commercial paste (30-NRD paste in ethanol) via spin coating with 5,000 rpm for 20 s and sintering using an stepwise annealing elevation ramp from room temperature to 480 °C (ref. 60). In addition, Li-TFSI treatment was performed via spin coating of Li-TFSI salt in acetonitrile (34.8 mM) solution on the as-prepared mp-TiO₂ surface by using 170 µl of the solution and 7 s loading time, followed by spin coating at 3,000 rpm for 10 s and sintering programme same as mp-TiO₂ and transferred to the glove box at 150 °C. The process for preparation of the mixed cation/halide perovskite solution (3D perovskite precursor) with triple-cation (TCP) Cs_{0.05}MA_{0.15}FA_{0.8}PbI_{2.53}Br_{0.47} composition involved mixing PbI₂:PbBr₂:FAI:MABr with 44:8:40:8 mol% in DMF/DMSO (4:1 vol%) followed by addition of 59 µl solution of CsI (1.5 M in DMSO) in 1 ml perovskite solution. An 80 µl of solution was spin-coated in a two-step programme, including 10 s at 1,000 rpm with a ramp of 200 rpm and 5,000 rpm with a ramp of 2,000 rpm for 20 s, respectively. During the second step, 200 µl CB was poured on the spinning substrate and the substrates were annealed at 100 °C for 60 min, while DCP solution was made by mixing PbI₂:PbBr₂:FAI:MACl:MABr with 44:2:40:12:2 mol% in DMF/DMSO (4:0.8 vol%) and final composition of MA_{0.10}FA_{0.90}PbI_{2.66}Br_{0.09}Cl_{0.25}. Perovskite (70 µl) was deposited on the substrate via the spin-coating process for 10 s at 1,000 rpm with a ramp of 200 rpm and 5,000 rpm with a ramp of 2,000 rpm for 25 s, respectively, and in the second step, 600 µl DEE was poured on the substrate and sintered at 150 °C for 10 min and at 100 °C for 10 min to form the perovskite film. The composition of the TCP and DCP layers was adopted based on our previous optimizations for each composition to have well surface coverage, film quality and PV performances.

Subsequently, the 2D perovskite layer was formed via spin coating of 80 µl BGA solution in CB (80 mM as optimized concentration) at 5,000 rpm for 35 s and annealing at 100 °C for 10 min. Solution (0.051 mM) of ultra-high-molecular-weight 390 kDa PTAA in CB was prepared, and it was doped with Li-TFSI (1.8 M in acetonitrile), TBP and FK209-Co(III)-TFSI (0.14 M in acetonitrile) with a ratio of 20:78:2 mol%. The PTAA solution was stirred for 3 h at room temperature⁶⁸ and deposited on the 3D/2D perovskite layer via spin coating at 6,000 rpm for 45 s. Finally, 100 nm gold was deposited on the substrates via a vacuum metal evaporator.

Module fabrication

A P1–P2–P3 laser patterning was adopted by means of an Nd:YVO₄ ns laser ($\lambda = 355$ nm). For the medium-size modules, each module consists of 5 series-connected cells, with cell width of 5 mm and 36 mm length with a 9.0 cm² active area (91% GFF), while for the large-area module, 15 series-connected cells with an active area of 48 cm² (89% GFF) were patterned on a large FTO substrate. A raster scanning laser (Nd:YVO₄ pulsed at 80 kHz) was applied to etch the FTO/glass substrates. FTO

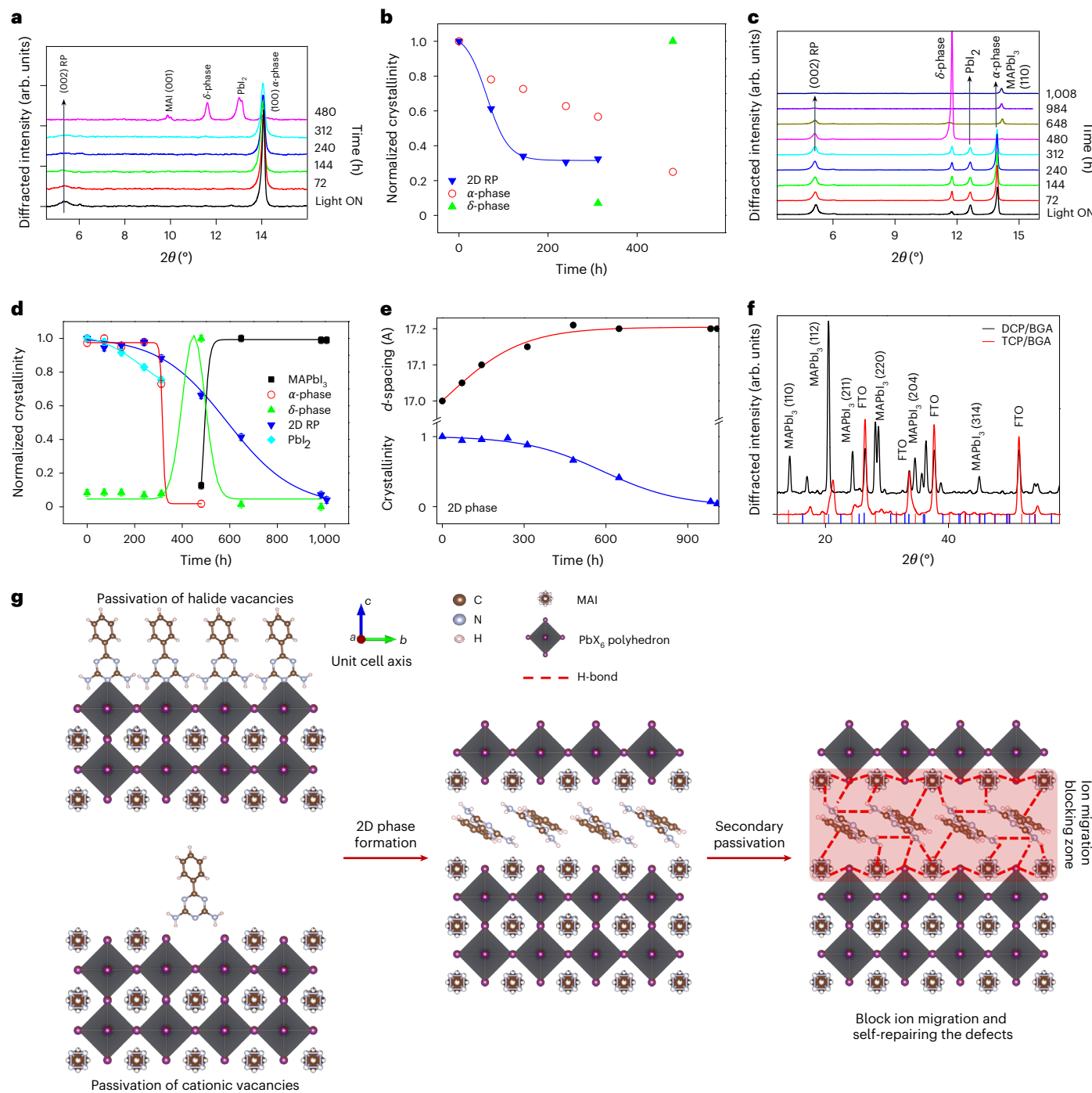


Fig. 5 | Stability mechanisms of 3D/2D PSCs: a structural and kinetic analysis.

a,b, Low-angle XRD patterns (a) and time evolution of the crystallinity of the various perovskite phases (via Gaussian fitting of XRD data of the DCP/BGA film), as obtained by sigmoidal fitting of XRD data (blue line, $A_1 = 1.050$; $A_2 = 0.316$; $x_0 = 62.8$ h; $d_x = 24.0$ h) (b) collected upon the surface of the TCP/BGA film at different ageing times. **c,d**, Low-angle XRD patterns (c) and time evolution of the crystallinity of the various perovskite phases (fit details; sigmoidal MAPbI_3 (black line), $A_1 = 0.000$; $A_2 = 1.000$; $x_0 = 491.8$ h; $d_x = 11.0$ h; sigmoidal α -phase (red line), $A_1 = 1.000$; $A_2 = 0.018$; $x_0 = 317.5$ h; $d_x = 5.1$ h; Gaussian δ -phase (green line), $y_0 = 0.05$; $x_0 = 448.3$ h; $w = 95.5$ h; sigmoidal 2D RP (blue line), $A_1 = 1.000$; $A_2 = 0.004$; $x_0 = 588.3$ h; $d_x = 141.8$ h; sigmoidal PbI_2 (cyan line), $A_1 = 1.030$; $A_2 = 0.640$; $x_0 = 230.5$ h; $d_x = 93.6$ h), as obtained by Gaussian fitting

of XRD data (d) collected upon the surface of the DCP/BGA film at different ageing times (collected from 60 independent variables). The error bars of each measured time are presented in the graph. **e**, Time evolution of the lattice parameter value for the 2D phase. Sigmoidal fit of crystallinity (blue line, $A_1 = 1.007$; $A_2 = 0.004$; $x_0 = 588.3$ h; $d_x = 141.8$ h) and lattice parameter (red line, $A_1 = 16.025$ (A); $A_2 = 17.204$ (A); $x_0 = 19.7$ h; $d_x = 137.0$ h). **f**, XRD patterns collected upon DCP/BGA and TCP/BGA samples at the end of ageing (1,048 h). Red and blue bars correspond to theoretical peak positions of α and δ perovskite 3D phases. **g**, Multifunctional primary and secondary surface passivation mechanisms using a BGA overlayer. The arbitrary units labelled as 'arb. units'.

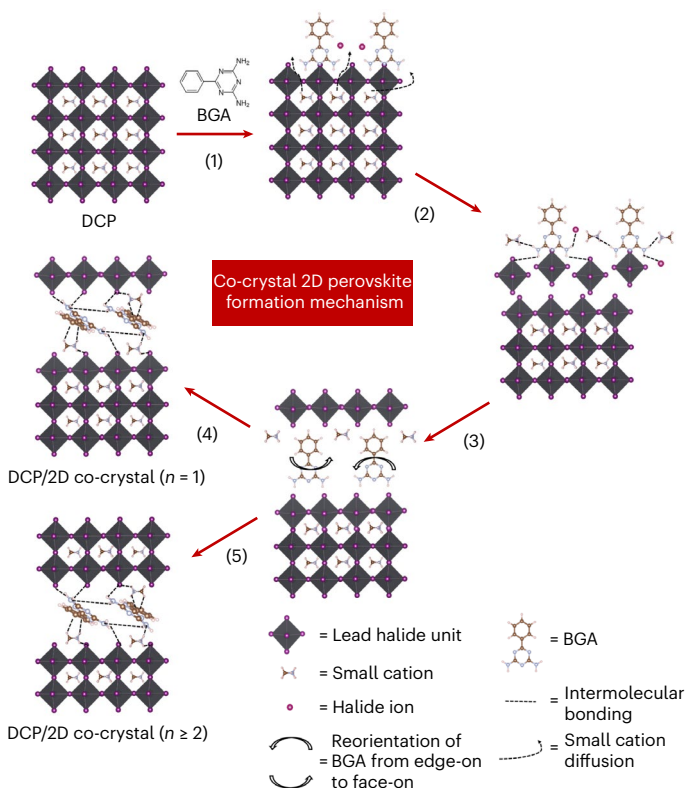


Fig. 6 | Schematic representing the co-crystal 2D perovskite overlayer phase formation mechanism on the DCP layer. The mechanism including multiple steps, including ligand exchange reaction (1), intermolecular stabilization and initial layer disruption (2), lead halide chain reformation (3), BGA reorientation and 2D perovskite formation (4) and layer-by-layer growth (5).

substrates were first cleaned with detergent (Hellmanex III (5%V) in ionized water), distilled water and isopropyl alcohol (5 min for each step via ultrasonic bath), and then the P1 process was applied, with a fluence of 1.95 J cm^{-2} , to insulate the FTO layer of neighbouring cells. Then, the substrates were kept on a hot plate, reaching 460°C in 35 min, and the c-TiO₂ layer was deposited with the same procedure of the small-area cells. Mesoporous TiO₂ paste was diluted in ethanol (1:7, w/w) and deposited by spin coating at 5,000 rpm for 10 s (medium modules) and (1:6.5 w/w TiO₂ paste in ethanol) at 4,000 rpm for 15 s (large module), followed by the stepwise annealing programme, which was utilized for the small-area cells. The Li-TFSI in acetonitrile solution (0.034 M) was deposited on the mp-TiO₂ layer by spin coating with loading time for 7 s at 3,000 rpm for 10 s (medium modules) and 2,000 rpm for 10 s (large module), and subsequently sintered with the same annealing programme of the mesoporous layer. The substrates were immediately transferred to the N₂-filled glove box, while the temperature cooled to 150°C to perform perovskite deposition.

The 3D perovskite (DCP) solution was deposited on the substrate via the zero-waste blade-spin method¹⁶. In brief, 40 μl (80 μl for large-area module) of the 3D perovskite solution (same concentration of the small-area cells) was blade-coated at room temperature with 1 mm s^{-1} speed and 400 μm (500 μm for large-area module) blade distance. Then, the wet perovskite layer was spin-coated at 4,000 rpm for 10 s and DEE was poured on the substrate during the spin coating.

The substrates then were transferred on a hot plate for sintering at 150°C for 10 min and 100°C for 10 min. The co-crystal 2D perovskite layer was deposited via blade coating of 30 μl (60 μl for large-area module) BGA in CB solution (same concentration of the small-area cells) at room temperature with 0.1 mm s^{-1} speed and 250 μm (350 μm for large-area module) blade distance. Then, the substrates were annealed at 100°C for 10 min.

An ultra-high-molecular-weight PTAA solution same as small-area cells was deposited on the 3D/2D perovskite layer via spin coating at 5,000 rpm for medium module (4,000 rpm for the large module with a ramp of 2,000 rpm) for 45 s. After the deposition of hole transport material (HTM) layers, the P2 patterning process (fluence of 117.7 mJ cm^{-2}) was applied to remove the electron transport layer–perovskite–hole transport layer stack from the underneath FTO, and realize vertical contacts between the latter and the subsequently deposited electrode. Finally, 115 nm gold was deposited via evaporation. After the gold evaporation, the P3 laser patterning (fluence of 224 mJ cm^{-2}) step was realized to insulate the counter-electrodes of the single cells.

Modules for light soaking stability tests have been encapsulated using materials compatible with the production environment by means of an industrial hot vacuum laminator (Core 2 by Rise Technology). The 0.5 mm sheet ionomer (Jurasol from Juraplast) and butyl cordons (HelioSeal PV 101 from Kommerling) have been used respectively as primary and edge sealing to encapsulate the PV modules. Lamination processes have been adapted to limit the max temperature that may damage the active layers of the realized PV modules. A progressive 130°C process developed by Greatcell Solar Italia Srl has been adopted for lamination and external contacts are made using tabbing ribbons fixed on the positive and negative poles of the PV module by means of conductive copper tapes.

For the thermal stability and UV exposure tests, we used glass/glass encapsulation process by using Helioseal 101 butyl cordons as the edge sealants and hot pressing under vacuum (100°C temperature and 0.5 bar pressure). Stainless steel tape has been used for transferring of the contacts, and the external edges have been covered by polytetrafluoroethylene tape and epoxy resin.

Thin-film sample fabrication

FTO substrates with a $2.5 \times 2.5 \text{ cm}^2$ area were cleaned using the same aforementioned process of the small-area cells. A thin film of mp-TiO₂ was deposited on the surface using the same process of the small-area cells and used as a substrate for deposition of all the 2D perovskite films.

Various deposition inks of the 2D perovskite layer have been fabricated by mixing different molar ratios of BGA, PbI₂ and MAI in DMF/DMSO (4:1 vol%) and deposited on the mesoscopic substrates via a two-step spin coating, including 10 s at 1,000 rpm with a ramp of 200 rpm and 4,000 rpm with a ramp of 2,000 rpm for 20 s, respectively. During the second step, 150 μl CB was poured on the spinning substrate and the substrates were annealed at 100°C for 10 min. The same process has been used for preparation of various deposition inks of BGA, AGA and PEAI with different mole ratios versus MAI and fixed amount of PbI₂ solution and fabrication of the low-dimensional perovskite thin films on glass substrates ($2.5 \times 2.5 \text{ cm}^2$), without any transparent conductive oxide and electron transport layer, by the same spin-casting process and annealing at 100°C for 20 min.

Measurement and instruments

The PV performance of the small-area devices and modules was analysed at atmospheric conditions (around 65% RH) via measurement of 0.1 cm^2 masked devices (20 mV s^{-1} and 50 mV s^{-1} voltage scan rate) under a solar simulator (ABET Sun 2000, class A) at AM1.5 G and 100 mW cm^{-2} illumination, which was calibrated with a certified reference Si cell (RERA Solutions RR-1002). The incident power was checked with a Skye SKS 1110 sensor. The morphological analysis was realized with a field emission scanning electron microscope (HR FESEM Zeiss Auriga Microscopy) and regular SEM using a TESCAN Analytics VEGA instrument. The absorbance spectra were analysed by using a UV-vis spectrometer (UV-2550, Shimadzu). The Incident-Photon-to-Current Efficiency curves were assessed by using Arkeo (Cicci Research) based on a 300 W xenon lamp and double grating (300–1,400 nm) and the correct integration of the incident monochromatic light was made comparing the photoresponse of a Si UV-enhanced NIST calibrated

photodetector. For the thermal stability tests, encapsulated modules put in an oven with 85 °C temperature and atmospheric condition (65% RH) and the PV performance were analysed regularly.

Light soaking stability was performed via a Cicci Research instrument at atmospheric condition (65% RH). The measurement system Arkeo multichannel platform with 32 fully independent source meters was used. MPP is tracked with a 3-point P&O algorithm and a $J-V$ scan is performed every 10 min to measure $J-V$ parameters such as J_{sc} , open-circuit voltage (V_{oc}), efficiency and FF. Light soaker, Arkeo LED-based light soaker (400–750 nm) with a 1-sun output power, was used. Intensity is calibrated by reaching the equivalent J_{sc} under a sun simulator. UV-ray exposure stability tests were performed using an extended Arkeo multichannel platform, illuminating encapsulated modules with UV light (300–400 nm, 4.51 mW cm⁻²) while tracking the MPP under continuous UV exposure and ambient atmospheric conditions (65% RH).

PL tests were performed with a commercial platform (Arkeo, Cicci Research). PL spectra were collected with an all-in-one platform (Arkeo from Cicci Research) where the substrate was placed on a thermal stage. Pump is provided by 405 nm or 532 nm diode-pumped solid-state (DPSS) Nd:YVO₄ + KTP lasers with optical power of 1 mW and 45° of inclination related to the substrate. From the same side of the lasers, PL was detected with a 10 mm of diameter aspheric lens close to the substrate and recorded by a charge-coupled device-based spectrometer. Integration time and number of averaging are maintained the same in order to better compare the results. Time-correlated single-photon counting was used to measure the PL decay (TRPL) behaviour of the fabricated cells using an Arkeo (Cicci Research) instrument. The device was illuminated with a 405 nm laser pulsing at 1 MHz with a full width at half maximum of 50 ps, synchronized to a single-photon avalanche diode photon counter. The resulting signal was detected by the SPAD detector after passing through a 480 nm low-pass filter and recorded to form the PL decay curve. A tri-exponential (DEC3 exp) function has been used for fitting of the TRPL curves. TPV and TPC were analysed with a commercial apparatus (Arkeo, Cicci Research s.r.l.) based on a high-speed waveform generator that drives a high-speed LED (5,000 kelvin). For the TPV, the tests were performed under a constant bias illumination, while the short light pulses, used to create the charge carriers, are very slight perturbations of this bias. The test is repeated ten times by increasing bias light intensity, and for each measurement, the maximum voltage is recorded. For the TPC, the device is illuminated with different bias light intensities. For each intensity, a $J-t$ curve is plotted and the decay curve is integrated over time. The resulting charge is then plotted versus the steady-state current density when the light is on. EIS was done by AUTOLAB at short circuit and 4 bias voltages (0.2 V, 0.4 V, 0.6 V and 0.8 V) and frequency range of 100 kHz to 0.1 Hz under dark condition, and the results were fitted by ZView v. 3.5h. Dark $J-V$ measurements were performed by AUTOLAB under dark condition in the voltage range of 0–1.2 V with 50 mV s⁻¹ as a scan rate. XRD measurements were performed in reflection mode on a Panalytical Empyrean diffractometer by means of $\text{K}\alpha$ fluorescence lines (K-Alpha₁(Å) = 1.54060; K-Alpha₂(Å) = 1.54443) of a Cu anode. For standard XRD measurements ($10^\circ < 2\theta < 70^\circ$), Bragg–Brentano configuration was used as an incident optical pathway focusing the impinging beam with fixed divergent slits (1/4°–1/2°). Low-angle acquisitions ($2.5^\circ < 2\theta < 20^\circ$) were obtained narrowing down the slit's dimensions to (1/32°–1/16°). A solid-state hybrid Pix'cel 3D detector, working in 1D linear mode, accomplished the detection and continuous scan mode was adopted. XRD measurements of the 3D + 2D-based films were performed by RIGAKU SmartLab SE in a Bragg–Brentano mode and low angle ($2\theta = 2$ –20°) using a fixed knife edge and high-resolution and ultrafast 1D X-ray detector D/teX Ultra250 (0/1D). SmartLab Studio II software were used for fitting the peaks. CIFs were used for detection of the low-dimensional perovskite peaks and PbI₂. GIWAXS data were acquired with a Bruker D8 Discover Plus diffractometer equipped with

a Dectris Eiger2 detector and a copper rotating anode. The beam was shaped with a 60 mm focusing Goebel mirror, followed by a 0.5 mm pinhole and a 0.3 mm double-pinhole collimator. The detector was positioned at approximately 117 mm in gamma-optimized orientation using an additional adapter plate to increase gamma coverage. Separate images were acquired for 600 s each at different 2θ positions and at incidence angle 2° omega. Images were then merged using Diffrac.EVA 6.0 and transformed to Q using GIXGUI⁶⁹. XPS measurements have been performed in ultra-high vacuum conditions at a base pressure lower than 2×10^{-10} mbar. Samples were not further treated after insertion in the vacuum chamber. Non-monochromatic Al $\text{K}\alpha$ radiation was used as X-ray source, and signals were monitored via a five-channeltron hemispherical electron analyser with a pass energy of 30 eV. Samples were at room temperature during all measurements.

Computational methods

DFT calculations were carried out using the Vienna Ab initio Simulation Package (VASP)⁷⁰. The generalized gradient approximation Perdew–Burke–Ernzerhof functional was used to account for the Kohn–Sham electron exchange correlation interactions⁷¹. The projector augmented wave method was used to represent the ionic cores⁷². The cut-off energy for bulk optimization was 520 eV, while 400 eV was set for surface geometry optimizations. Similarly, $8 \times 8 \times 8$ Monkhorst–Pack k -point meshes⁷³ was used for the bulk optimization, while $2 \times 2 \times 1$ was used for surface geometry optimizations. The break condition for self-consistent iterations was 1×10^{-5} , and the ion relaxation was stopped when the forces on all atoms were smaller than -0.05 eV Å⁻¹. The energy and geometry for gas-phase calculations were done by placing gas-phase molecules into a large box with dimensions of $20 \times 20 \times 20$ Å³. A single F -point was used for these calculations.

Reporting summary. Further information on research design is available in the Nature Portfolio Reporting Summary linked to this article.

Data availability

The data that support the findings of this study are available in the Article and its Supplementary Information. Source data are provided with this paper. These data are available via Zenodo at <https://doi.org/10.5281/zenodo.17334221> (ref. 74).

References

1. Zhang, F. et al. Advances in two-dimensional organic–inorganic hybrid perovskites. *Energy Environ. Sci.* **13**, 1154–1186 (2020).
2. Becker, M., Klüner, T. & Wark, M. Formation of hybrid ABX₃ perovskite compounds for solar cell application: first-principles calculations of effective ionic radii and determination of tolerance factors. *Dalton Trans.* **46**, 3500–3509 (2017).
3. Li, H. et al. Sensitive and stable 2D perovskite single-crystal X-ray detectors enabled by a supramolecular anchor. *Adv. Mater.* **32**, 2003790 (2020).
4. Ren, M., Cao, S., Zhao, J., Zou, B. & Zeng, R. Advances and challenges in two-dimensional organic–inorganic hybrid perovskites toward high-performance light-emitting diodes. *Nanomicro Lett.* **13**, 163 (2021).
5. Kim, E.-B., Akhtar, M. S., Shin, H.-S., Armeen, S. & Nazeeruddin, M. K. A review on two-dimensional (2D) and 2D–3D multidimensional perovskite solar cells: perovskites structures, stability, and photovoltaic performances. *J. Photochem. Photobiol. C* **48**, 100405 (2021).
6. Soe, C. M. M. et al. Structural and thermodynamic limits of layer thickness in 2D halide perovskites. *Proc. Natl Acad. Sci. USA* **116**, 58–66 (2019).
7. Ortiz-Cervantes, C., Carmona-Monroy, P. & Solis-Ibarra, D. Two-dimensional halide perovskites in solar cells: 2D or not 2D? *ChemSusChem* **12**, 1560–1575 (2019).

8. Huang, W., Bu, T., Huang, F. & Cheng, Y.-B. Stabilizing high efficiency perovskite solar cells with 3D-2D heterostructures. *Joule* **4**, 975–979 (2020).
9. Liu, Y. et al. Ultrahydrophobic 3D/2D fluoroarene bilayer-based water-resistant perovskite solar cells with efficiencies exceeding 22%. *Sci. Adv.* **5**, eaaw2543 (2019).
10. Cai, Y. et al. Graded 2D/3D $(CF_3\text{-PEA})_2\text{FA}_{0.85}\text{MA}_{0.15}\text{Pb}_2\text{I}_7/\text{FA}_{0.85}\text{MA}_{0.15}\text{PbI}_3$ heterojunction for stable perovskite solar cell with an efficiency over 23.0%. *J. Energy Chem.* **65**, 480–489 (2022).
11. Jeong, S. et al. Cyclohexylammonium-based 2D/3D perovskite heterojunction with funnel-like energy band alignment for efficient solar cells (23.91%). *Adv. Energy Mater.* **11**, 2102236 (2021).
12. Yang, J. et al. A review on improving the quality of perovskite films in perovskite solar cells via the weak forces induced by additives. *Appl. Sci.* **9**, 4393 (2019).
13. Su, L. et al. Performance enhancement of perovskite solar cells using trimesic acid additive in the two-step solution method. *J. Power Sources* **426**, 11–15 (2019).
14. Gunes, U. et al. A thienothiophene-based cation treatment allows semitransparent perovskite solar cells with improved efficiency and stability. *Adv. Funct. Mater.* <https://doi.org/10.1002/adfm.202103130> (2021).
15. Yoo, J. J. et al. An interface stabilized perovskite solar cell with high stabilized efficiency and low voltage loss. *Energy Environ. Sci.* **12**, 2192–2199 (2019).
16. Zendehdel, M., Yaghoobi Nia, N., Paci, B., Generosi, A. & Di Carlo, A. Zero-waste scalable blade-spin coating as universal approach for layer-by-layer deposition of 3D/2D perovskite films in high-efficiency perovskite solar modules. *Sol. RRL* <https://doi.org/10.1002/solr.202100637> (2021).
17. Sidhik, S. et al. Deterministic fabrication of 3D/2D perovskite bilayer stacks for durable and efficient solar cells. *Science* **377**, 1425–1430 (2022).
18. Li, C.-H., Liao, M.-Y., Chen, C.-H. & Chueh, C.-C. Recent progress of anion-based 2D perovskites with different halide substitutions. *J. Mater. Chem. C* **8**, 4294–4302 (2020).
19. Wu, T., Li, X., Qi, Y., Zhang, Y. & Han, L. Defect passivation for perovskite solar cells: from molecule design to device performance. *ChemSusChem* **14**, 4354–4376 (2021).
20. Li, D. et al. A review on scaling up perovskite solar cells. *Adv. Funct. Mater.* **31**, 2008621 (2021).
21. Yaghoobi Nia, N. et al. Beyond 17% stable perovskite solar module via polaron arrangement of tuned polymeric hole transport layer. *Nano Energy* **82**, 105685 (2021).
22. Yaghoobi Nia, N. et al. Solution-based heteroepitaxial growth of stable mixed cation/anion hybrid perovskite thin film under ambient condition via a scalable crystal engineering approach. *Nano Energy* **69**, 104441 (2020).
23. Park, N.-G. & Zhu, K. Scalable fabrication and coating methods for perovskite solar cells and solar modules. *Nat. Rev. Mater.* **5**, 333–350 (2020).
24. Yaghoobi Nia, N. et al. Doping strategy for efficient and stable triple cation hybrid perovskite solar cells and module based on poly(3-hexylthiophene) hole transport layer. *Small* **15**, 1904399 (2019).
25. Liu, C. et al. Tuning structural isomers of phenylenediammonium to afford efficient and stable perovskite solar cells and modules. *Nat. Commun.* **12**, 6394 (2021).
26. Bi, E. et al. Efficient perovskite solar cell modules with high stability enabled by iodide diffusion barriers. *Joule* **3**, 2748–2760 (2019).
27. Liu, Z. et al. A holistic approach to interface stabilization for efficient perovskite solar modules with over 2,000-hour operational stability. *Nat. Energy* **5**, 596–604 (2020).
28. Christians, J. A. et al. Stability at scale: challenges of module interconnects for perovskite photovoltaics. *ACS Energy Lett.* **3**, 2502–2503 (2018).
29. Yaghoobi Nia, N. et al. A crystal engineering approach for scalable perovskite solar cells and module fabrication: a full out of glove box procedure. *J. Mater. Chem. A* **6**, 659–671 (2018).
30. Zhao, L. et al. Redox chemistry dominates the degradation and decomposition of metal halide perovskite optoelectronic devices. *ACS Energy Lett.* **1**, 595–602 (2016).
31. Yu, P., Zhen, Y., Dong, H. & Hu, W. Crystal engineering of organic optoelectronic materials. *Chem* **5**, 2814–2853 (2019).
32. Ye, X. et al. 1D versus 2D cocrystals growth via microspacing in-air sublimation. *Nat. Commun.* **10**, 761 (2019).
33. Wang, Y. et al. in *Molecular-Scale Electronics* (ed. Guo, X.) 229–262 (Springer, 2019).
34. Park, K. et al. Preparation of covalent triazine frameworks with imidazolium cations embedded in basic sites and their application for CO_2 capture. *J. Mater. Chem. A* **5**, 8576–8582 (2017).
35. Khattab, S. N. et al. Design and synthesis of new s-triazine polymers and their application as nanoparticulate drug delivery systems. *New J. Chem.* **40**, 9565–9578 (2016).
36. Habibi, M. H., Zendehdel, M., Barati, K., Harrington, R. W. & Clegg, W. A 1:1 cocrystal of 4-(dimethylamino)benzaldehyde and 6-phenyl-1,3,5-triazine-2,4-diamine. *Acta Crystallogr. C* **63**, o474–o476 (2007).
37. Jeyanthi, G. & Gnana Sambandam, C. Spectral profiling, structural, molecular docking and ELF elucidation of bioactive molecule benzoguanamine. *J. Mol. Struct.* **1243**, 130879 (2021).
38. Yao, W., Song, N., Xie, J., Zhao, H. & Li, X. Solubility of acetoguanamine in twelve neat solvents from 283.15 to 323.15 K. *J. Chem. Eng. Data* **64**, 4546–4550 (2019).
39. Stoumpos, C. C. et al. Ruddlesden–Popper hybrid lead iodide perovskite 2D homologous semiconductors. *Chem. Mater.* **28**, 2852–2867 (2016).
40. Shibuya, K., Koshimizu, M., Nishikido, F., Saito, H. & Kishimoto, S. Poly[bis(phenethylammonium) [dibromidoplumbate(II)]-di-u-bromido]. *Acta Crystallogr. E* **65**, m1323–m1324 (2009).
41. Bartlett, P. N. et al. Haloplumbate salts as reagents for the non-aqueous electrodeposition of lead. *RSC Adv.* **6**, 73323–73330 (2016).
42. Lorena, G. S., Hasegawa, H., Takahashi, Y., Harada, J. & Inabe, T. Hole doping of tin bromide and lead bromide organic–inorganic hybrid semiconductors. *Chem. Lett.* **43**, 1535–1537 (2014).
43. Fu, W. et al. Tailoring the functionality of organic spacer cations for efficient and stable quasi-2D perovskite solar cells. *Adv. Funct. Mater.* **29**, 1900221 (2019).
44. Li, M.-H. et al. Highly efficient 2D/3D hybrid perovskite solar cells via low-pressure vapor-assisted solution process. *Adv. Mater.* **30**, 1801401 (2018).
45. Cordero, F. et al. Stability of cubic FAPbI_3 from X-ray diffraction, anelastic, and dielectric measurements. *J. Phys. Chem. Lett.* **10**, 2463–2469 (2019).
46. Cordero, F. et al. Influence of temperature, pressure, and humidity on the stabilities and transition kinetics of the various polymorphs of FAPbI_3 . *J. Phys. Chem. C* **124**, 22972–22980 (2020).
47. Liang, C. et al. Ruddlesden–Popper perovskite for stable solar cells. *Energy Environ. Mater.* **1**, 221–231 (2018).
48. Schlipf, J. et al. Shedding light on the moisture stability of 3D/2D hybrid perovskite heterojunction thin films. *ACS Appl. Energy Mater.* **2**, 1011–1018 (2019).
49. Li, X. et al. Two-dimensional Dion–Jacobson hybrid lead iodide perovskites with aromatic diammonium cations. *J. Am. Chem. Soc.* **141**, 12880–12890 (2019).

50. Chen, P. et al. In situ growth of 2D perovskite capping layer for stable and efficient perovskite solar cells. *Adv. Funct. Mater.* **28**, 1706923 (2018).
51. Lee, M.-S., Park, M., Kim, H. Y. & Park, S.-J. Effects of microporosity and surface chemistry on separation performances of N-containing pitch-based activated carbons for CO₂/N₂ binary mixture. *Sci. Rep.* **6**, 23224 (2016).
52. Kumar, S. N., Boussoux, G. & Gaillard, F. Electronic and structural characterization of electrochemically synthesized conducting polyaniline from XPS studies. *Surf. Interface Anal.* **15**, 531–536 (1990).
53. Lin, Y.-P. et al. Self-assembled melamine monolayer on Cu(111). *J. Phys. Chem. C* **117**, 9895–9902 (2013).
54. Wang, Y. et al. Stitching triple cation perovskite by a mixed anti-solvent process for high performance perovskite solar cells. *Nano Energy* **39**, 616–625 (2017).
55. Shi, D. et al. Low trap-state density and long carrier diffusion in organolead trihalide perovskite single crystals. *Science* **347**, 519–522 (2015).
56. Stewart, R. J., Grieco, C., Larsen, A. V., Maier, J. J. & Asbury, J. B. Approaching bulk carrier dynamics in organo-halide perovskite nanocrystalline films by surface passivation. *J. Phys. Chem. Lett.* **7**, 1148–1153 (2016).
57. Krückemeier, L., Krogmeier, B., Liu, Z., Rau, U. & Kirchartz, T. Understanding transient photoluminescence in halide perovskite layer stacks and solar cells. *Adv. Energy Mater.* **11**, 2003489 (2021).
58. Guerrero, A. et al. Properties of contact and bulk impedances in hybrid lead halide perovskite solar cells including inductive loop elements. *J. Phys. Chem. C* **120**, 8023–8032 (2016).
59. Abdulrahim, S. M., Ahmad, Z., Bhadra, J. & Al-Thani, N. J. Long-term stability analysis of 3D and 2D/3D hybrid perovskite solar cells using electrochemical impedance spectroscopy. *Molecules* **25**, 5794 (2020).
60. Liao, P., Zhao, X., Li, G., Shen, Y. & Wang, M. A new method for fitting current–voltage curves of planar heterojunction perovskite solar cells. *Nanomicro Lett.* **10**, 5 (2018).
61. Sherkar, T. S. et al. Recombination in perovskite solar cells: significance of grain boundaries, interface traps, and defect ions. *ACS Energy Lett.* **2**, 1214–1222 (2017).
62. Khenkin, M. V. et al. Consensus statement for stability assessment and reporting for perovskite photovoltaics based on ISOS procedures. *Nat. Energy* **5**, 35–49 (2020).
63. Deng, Y., Xiao, Z. & Huang, J. Light-induced self-poling effect on organometal trihalide perovskite solar cells for increased device efficiency and stability. *Adv. Energy Mater.* **5**, 1500721 (2015).
64. Reinoso, M. Á., Otálora, C. A. & Gordillo, G. Improvement properties of hybrid halide perovskite thin films prepared by sequential evaporation for planar solar cells. *Materials* **12**, 1394 (2019).
65. Chen, B., Rudd, P. N., Yang, S., Yuan, Y. & Huang, J. Imperfections and their passivation in halide perovskite solar cells. *Chem. Soc. Rev.* **48**, 3842–3867 (2019).
66. Campos, T. et al. Unraveling the formation mechanism of the 2D/3D perovskite heterostructure for perovskite solar cells using multi-method characterization. *J. Phys. Chem. C* **126**, 13527–13538 (2022).
67. Sardashti, M. K., Zendehdel, M., Nia, N. Y., Karimian, D. & Sheikhi, M. High efficiency MAPbI₃ perovskite solar cell using a pure thin film of polyoxometalate as scaffold layer. *ChemSusChem* **10**, 3773–3779 (2017).
68. Yaghoobi Nia, N. et al. Analysis of the efficiency losses in hybrid perovskite/PTAA solar cells with different molecular weights: morphology versus kinetics. *ACS Appl. Energy Mater.* **3**, 6853–6859 (2020).
69. Jiang, Z. *GI/XSGUI*: a MATLAB toolbox for grazing-incidence X-ray scattering data visualization and reduction, and indexing of buried three-dimensional periodic nanostructured films. *J. Appl. Crystallogr.* **48**, 917–926 (2015).
70. Kresse, G. & Furthmüller, J. Efficient iterative schemes for ab initio total-energy calculations using a plane-wave basis set. *Phys. Rev. B* **54**, 11169–11186 (1996).
71. Perdew, J. P., Burke, K. & Ernzerhof, M. Generalized gradient approximation made simple. *Phys. Rev. Lett.* **77**, 3865–3868 (1996).
72. Blöchl, P. E. Projector augmented-wave method. *Phys. Rev. B* **50**, 17953–17979 (1994).
73. Monkhorst, H. J. & Pack, J. D. Special points for Brillouin-zone integrations. *Phys. Rev. B* **13**, 5188–5192 (1976).
74. Yaghoobi Nia, N. Cocrystal engineering of 2D perovskite phase for perovskite solar modules with improved efficiency and stability. Zenodo <https://doi.org/10.5281/zenodo.1733422> (2025).
75. Deng, Y. et al. Defect compensation in formamidinium–caesium perovskites for highly efficient solar mini-modules with improved photostability. *Nat. Energy* **6**, 633–641 (2021).
76. Zeng, H. et al. Improved performance and stability of perovskite solar modules by regulating interfacial ion diffusion with nonionic cross-linked 1D lead-iodide. *Adv. Energy Mater.* **12**, 2102820 (2022).
77. Zhang, S. et al. Improved performance and stability of perovskite solar modules by interface modulating with graphene oxide crosslinked CsPbBr₃ quantum dots. *Energy Environ. Sci.* **15**, 244–253 (2022).
78. Yang, Z. et al. Slot-die coating large-area formamidinium–cesium perovskite film for efficient and stable parallel solar module. *Sci. Adv.* **7**, eabg3749 (2021).
79. Kobayashi, E., Tsuji, R., Martineau, D., Hinsch, A. & Ito, S. Light-induced performance increase of carbon-based perovskite solar module for 20-year stability. *Cell Rep. Phys. Sci.* **2**, 100648 (2021).
80. Jiang, Y. et al. Negligible-Pb-waste and upscalable perovskite deposition technology for high-operational-stability perovskite solar modules. *Adv. Energy Mater.* **9**, 1803047 (2019).

Acknowledgements

N.Y.N. gratefully acknowledges the Ministry of University and Research (MUR) for PON/FSE-REACT EU. M.Z. and A.D.C. gratefully acknowledge the funding from the Ministry of University and Research (MUR) with PRIN project CONPER (2022CBBEHN). J.X. and C.L. acknowledge the funding from the United States Department of Energy (US DOE), Office of Fossil Energy and Carbon Management (FECM) (contract number TCF-20-24815) under the Horizon 2020 (ERA-NET ACT 2021, NEXTCCUS project). N.Y.N. acknowledges P. Schouwink (platform leader at EPFL SB ISIC-XRDSAP) for his support for extraction of the GIWAXS results. The computational effort in this work was done utilizing computational resources provided by the Laboratory Computing Research Center (LCRC) at the Argonne National Laboratory.

Author contributions

M.Z. and N.Y.N. conceived the idea, methodology and conceptualization and M.Z. and N.Y.N. conducted devices and modules fabrication and optimization processes. N.Y.N. performed the encapsulation of modules for thermal stability and UV exposure tests. N.Y.N. conducted the laser patterning procedures. M.Z. and N.Y.N. fabricated all the samples for PL, XRD, GIWAXS, XPS, SEM, UV-vis absorbance spectroscopy and diffuse reflectance spectroscopy measurements. M.Z. performed the SEM measurements. M.Z. performed the EIS and dark J–V measurements and relevant

discussion. M.Z. and N.Y.N. performed the PL, UV-vis absorbance spectroscopy and diffuse reflectance spectroscopy measurements and TRPL, TPV and TPC measurements from the cells and fitting the relevant results. M.Z. performed the IV measurements for all devices and modules. M.Z. and N.Y.N. also conducted the XRD analyses of the 3D+2D and 3D/2D thin films formed on the glass substrates. M.Z. and N.Y.N. performed the stability assessments of the modules under light, UV-ray and thermal stresses. B.P., A.G. and M. Guaragno conducted the X-ray analysis and stability test via X-ray analysis and relevant discussion. E.L. encapsulated the medium-size modules for the light soaking tests. M.D.G. and G.C. performed the XPS analysis and relevant discussion. J.X. and C.L. performed the DFT computations and relevant discussion. M.Z. and N.Y.N. supervised the work. A.D.C. suggested the research topic. M.Z. and N.Y.N. prepared the original draft. M. Grätzel and all the authors contributed to the review and editing of the paper. All authors have read and agreed to the published version of the paper.

Competing interests

N.Y.N. is president and co-founder of IRITALY Trading Company S.r.l., a company that part of its activity is commercializing perovskite photovoltaics. E.L. is a senior researcher employer of Halocell Europe Srl (formerly known as Greatcell Solar Italia Srl), a company commercializing solar-grade materials. The other authors declare no competing interests.

Additional information

Supplementary information The online version contains supplementary material available at <https://doi.org/10.1038/s41560-025-01903-9>.

Correspondence and requests for materials should be addressed to Narges Yaghoobi Nia, Mahmoud Zendehdel or Aldo Di Carlo.

Peer review information *Nature Energy* thanks Fei Zhang and the other, anonymous, reviewer(s) for their contribution to the peer review of this work.

Reprints and permissions information is available at www.nature.com/reprints.

Publisher's note Springer Nature remains neutral with regard to jurisdictional claims in published maps and institutional affiliations.

Springer Nature or its licensor (e.g. a society or other partner) holds exclusive rights to this article under a publishing agreement with the author(s) or other rightsholder(s); author self-archiving of the accepted manuscript version of this article is solely governed by the terms of such publishing agreement and applicable law.

© The Author(s), under exclusive licence to Springer Nature Limited 2025

Solar Cells Reporting Summary

Nature Portfolio wishes to improve the reproducibility of the work that we publish. This form is intended for publication with all accepted papers reporting the characterization of photovoltaic devices and provides structure for consistency and transparency in reporting. Some list items might not apply to an individual manuscript, but all fields must be completed for clarity.

For further information on Nature Research policies, including our [data availability policy](#), see [Authors & Referees](#).

► Experimental design

Please check the following details are reported in the manuscript, and provide a brief description or explanation where applicable.

1. Dimensions

Area of the tested solar cells

Yes
 No

Total device active area: 9.0 cm² for the medium-size modules (5 series connected cells with 0.5 cm width and 3.6 cm lengths of each cell) and 48 cm² for the large area module (15 series connected cells with 0.459 cm width and 7.0 cm lengths of each cell).

Explain why this information is not reported/not relevant.

Method used to determine the device area

Yes
 No

Confocal microscopy (more details for the active area measurement of the modules can be found in the Supplementary Figure 19).

Explain why this information is not reported/not relevant.

2. Current-voltage characterization

Current density-voltage (J-V) plots in both forward and backward direction

Yes
 No

See Figure 3(c) and 4(c)

Voltage scan conditions

Yes
 No

Voltage scanned in both forward (0 to Voc) and reverse (Voc to 0) with following scan rates for cells and modules:
 cells: 20 mV/s and 50 mV/s, medium-size modules: 200 mV/s and large area module: 400 mV/s

Explain why this information is not reported/not relevant.

Test environment

Yes
 No

Photovoltaic performance of the small area devices and modules was analysed at atmospheric conditions (around 65% R.H.)

Explain why this information is not reported/not relevant.

Protocol for preconditioning of the device before its characterization

Yes
 No

All the non-encapsulated devices stored in a desiccator under 0.1 atmosphere vacuum while those were kept under atmospheric conditions during the measurement.
 The encapsulated modules stored under ambient conditions.

Explain why this information is not reported/not relevant.

Stability of the J-V characteristic

Yes
 No

MPP Tracking of the cells and modules under 1sun irradiation and atmospheric conditions (65% R.H.).

Explain why this information is not reported/not relevant.

3. Hysteresis or any other unusual behaviour

Description of the unusual behaviour observed during the characterization

Yes
 No

Hysteresis indexes of the statistics measurements have been evaluated via voltage scan in both forward and reverse directions

Explain why this information is not reported/not relevant.

Related experimental data

Yes
 No

The devices did not show any unusual behaviour

Explain why this information is not reported/not relevant.

4. Efficiency

External quantum efficiency (EQE) or incident photons to current efficiency (IPCE)

Yes
 No

The IPCE curves were assessed on a 300 W Xenon lamp and double grating (300–1400 nm) and the correct integration of the incident monochromatic light was made comparing the photoresponse of a Si UV-enhanced NIST calibrated photodetector.

Explain why this information is not reported/not relevant.

A comparison between the integrated response under the standard reference spectrum and the response measure under the simulator

Yes
 No

The champion device's IPCE plot (Supplementary Figure 16) shows good agreement between extracted current density and the J_{sc} from the J-V plot (See Page 14–15).

Explain why this information is not reported/not relevant.

For tandem solar cells, the bias illumination and bias voltage used for each subcell

Yes
 No

Provide a description of the measurement conditions.

We are not reporting any tandem structure

5. Calibration

Light source and reference cell or sensor used for the characterization

Yes
 No

solar simulator (ABET Sun 2000, class A) at AM 1.5G and 100 mW/cm² illumination which was calibrated with a certified reference Si Cell (RERA Solutions RR-1002)

Explain why this information is not reported/not relevant.

Confirmation that the reference cell was calibrated and certified

Yes
 No

The incident power was checked with a Skye SKS 1110 sensor

Explain why this information is not reported/not relevant.

Calculation of spectral mismatch between the reference cell and the devices under test

Yes
 No

Well matching between extracted current density to J_{sc} value of the JV plot

Explain why this information is not reported/not relevant.

6. Mask/aperture

Size of the mask/aperture used during testing

Yes
 No

Mask aperture area: 0.1 cm² for the cells; 9.9 cm² for the medium-size modules and 53.97 cm² for the large area module.

Explain why this information is not reported/not relevant.

Variation of the measured short-circuit current density with the mask/aperture area

Yes
 No

Well matching between extracted current density to J_{sc} value of the JV plot which characterized from masked cell

Explain why this information is not reported/not relevant.

7. Performance certification

Identity of the independent certification laboratory that confirmed the photovoltaic performance

Yes
 No

Identify the independent certification laboratory.

We are not reporting any efficiency record

A copy of any certificate(s)

Yes
 No

Certificate copies should be provided in the Supplementary information. Please state the supplementary item number.

We are not reporting any efficiency record

8. Statistics

Number of solar cells tested

Yes
 No

cells: The statistic results obtained from 12 cells of each structure fabricated in three batches (see Figure 3(b), Supplementary Figure 15 and Table 1). The box plots presented as SD range with Coef. of 1 and Whisker in the outlier range and Coef. of 1.5. The Mean, Min/Max and 1%/99% percentages have been shown by , – and × symbols, respectively.;

Modules: The statistic PCE data obtained from 4 independent modules for each studied configuration (see Figure 4(b), Supplementary Figure 20 and Table 2). The box plots presented as SD range with Coef. of 1 and Whisker in the outlier range and Coef. of 1.5. The Mean, Min/Max and 1%/99% percentages have been shown by , – and × symbols, respectively.;

Thermal stability of Modules: The statistic PCE data (see Figure 4(d) and Supplementary Figure 22) obtained from 2 independent modules (the mean point and error bars of each measured time are presented in the statistic graph).

Explain why this information is not reported/not relevant.

Statistical analysis of the device performance

Yes
 No

See pages 14 and 19

Explain why this information is not reported/not relevant.

9. Long-term stability analysis

Type of analysis, bias conditions and environmental conditions

Yes
 No

Encapsulated medium-size modules were tested with following conditions:
Light soaking stability was performed at atmospheric condition (65% R.H.). MPP is tracked with a 3-point P&O algorithm. Light soaker: Arkeo LED based light soaker (400-750 nm) with a 1-sun output power. Intensity is calibrated by reaching the equivalent J_{SC} under sun simulator.
Damp/Heat stability test: 85 °C at ambient atmospheric conditions (~R.H.: 65%); UV-ray exposure stability tests were performed using an extended Arkeo multichannel platform, illuminating encapsulated modules with UV light (300-400 nm, 4.51 mW/cm²) while tracking the maximum power point (MPP) under continuous UV exposure and ambient atmospheric conditions (65% R.H.).

Explain why this information is not reported/not relevant.